Article:
Heaton, T.J., Bard, E., Bronk Ramsey, C. et al. (2021) Radiocarbon : a key tracer for studying Earth's dynamo, climate system, carbon cycle, and Sun. Science, 374 (6568). abd7096. ISSN: 0036-8075

https://doi.org/10.1126/science.abd7096

Radiocarbon: a key tracer for studying the Earth's dynamo, climate system, carbon cycle and Sun

Enhanced Abstract

Background

Radiocarbon (^{14}C) has long been recognized as providing an essential dating technique covering the last 55,000 years. However, the further role of ^{14}C as a diagnostic tracer throughout the Earth and climate system is often less widely appreciated. Radiocarbon is formed by cosmic particles and then dispersed across multiple Earth system compartments. Consequently, accurate knowledge of past ^{14}C levels directly enables new discoveries, and provides connections, across broad research areas. We present recent advances in knowledge of past ^{14}C and the resulting insights that improve understanding of climate processes, solar activity, geophysics, and the carbon cycle. Measurements providing improved resolution in the variations of ^{14}C enable us to learn more about how these system components operate and interact.

Advances

Recent years have seen a revolution in our ability to reconstruct detailed records of ^{14}C. Advances include an explosion in measurements of single-year samples made possible by Accelerator Mass Spectrometry (AMS) instrumentation; new detail of pre-Holocene ^{14}C levels through use of speleothems, lake macrofossils and subfossil trees; and improved modeling of marine radiocarbon reservoir ages to incorporate carbon cycle changes. Combined with advanced statistical methods, these developments have allowed the IntCal working group to estimate ^{14}C levels with unprecedented accuracy for the Northern and Southern Hemispheres, as well as the surface ocean, back to the limit of the technique ~55,000 years ago.

Accompanying this, interdisciplinary studies have provided a new framework in which to use such comprehensive ^{14}C estimates. From the climate perspective, ^{14}C provides not only a chronology in which to place and compare diverse paleoclimate records, but also constraints on key climate forcings, such as solar variations, and changes in the carbon cycle.

Radiocarbon production is modulated by magnetic properties of solar wind, leading to lower production during high solar activity phases, and making atmospheric ^{14}C a mirror of solar activity. Conversely, brief ^{14}C production maxima have recently been identified and attributed to short-term solar energetic particle bursts. Comparisons of ^{14}C with other cosmogenic isotopes, such as ^{10}Be and ^{36}Cl in polar ice cores, allow significant progress in documenting past behavior of the Sun, previously poorly understood by astronomers. These recent astrophysical discoveries are important beyond academia since rapid solar and space weather events could severely damage current technology.

Radiocarbon also enables insight into the Earth's magnetic field, from the near-reversal of the Laschamps Excursion through to smaller perturbations including the drop over the last centuries. Again, comparison with other cosmogenic isotopes provides key inferences concerning paleomagnetic variations, which are still difficult to simulate with geodynamo models.

Finally, ^{14}C offers increased understanding of the carbon cycle and its feedbacks and responses to climate change. Radiocarbon permits the identification of CO_2 fluxes such as release of permafrost carbon. It also enables insight into the ocean's role in climate change via estimation of changes in the residence time of the carbon within it, and changes in the meridional overturning circulation during abrupt climate events.

Outlook

Harnessing ^{14}C's full potential involves addressing some key challenges. Current reconstructions of environmental ^{14}C rely upon a synthesis of measurements most of which only indirectly record atmospheric levels. The search for a fully-atmospheric reconstruction extending back 55,000 years of sufficient resolution continues. Such a development would greatly enhance our ability to independently test and validate climate and carbon cycle models.

Additionally, while significant periods of the record are now annually resolved, in other periods the temporal resolution is much coarser. A continuous annual atmospheric ^{14}C record would enable examination of long-term trends in solar activity and provide insight into the nature and frequency of shorter-lived space weather events.

Further, accompanying improvements in our records of other cosmogenic nuclides and paleomagnetic reconstructions, in combination with modeling advances, will allow identification of key feedbacks within our Earth and climate system. This will elucidate causal chains and permit testing of key hypotheses, resulting in improved predictions of climate change.

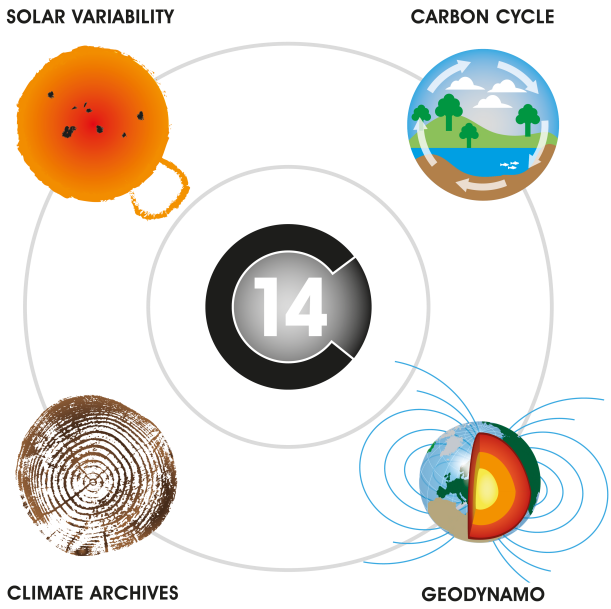

***Radiocarbon provides a unique link across diverse areas of research**. Knowledge of past ^{14}C levels provides insight into solar activity, the carbon cycle, and the geodynamo. It also enables the synchronised dating of key environmental records that are fundamental for the study of climate. As our estimates of past ^{14}C variation become more detailed and precise, we improve our understanding of the Earth and climate system.*

Radiocarbon: a key tracer for studying the Earth's dynamo, climate system, carbon cycle and Sun

Authors: T. J. Heaton[1]*, E. Bard[2], C. Bronk Ramsey[3], M. Butzin[4], P. Köhler[4], R. Muscheler[5], P. J. Reimer[6], L. Wacker[7]

Affiliations:

[1]School of Mathematics and Statistics, University of Sheffield, Sheffield S3 7RH, UK.

[2]CEREGE, Aix-Marseille University, CNRS, IRD, INRAE, Collège de France, Technopole de l'Arbois BP 80, 13545 Aix en Provence Cedex 4, France.

[3]Research Laboratory for Archaeology and the History of Art, University of Oxford, 1 South Parks Road, Oxford OX1 3TG, UK.

[4]Alfred-Wegener-Institut Helmholtz-Zentrum für Polar -und Meeresforschung (AWI), D-27515 Bremerhaven, Germany.

[5]Quaternary Sciences, Department of Geology, Lund University, Sölvegatan 12, 223 62 Lund, Sweden.

[6]The ^{14}CHRONO Centre for Climate, the Environment and Chronology, School of Natural and Built Environment, Queen's University Belfast BT7 1NN, UK.

[7]Laboratory of Ion Beam Physics, ETH, Otto-Stern-Weg 5, CH-8093 Zurich, Switzerland.

*Correspondence to: t.heaton@shef.ac.uk.

ORCID:

T J Heaton ORCID: https://orcid.org/0000-0002-9994-142X

E Bard ORCID: https://orcid.org/0000-0002-7237-8622

C Bronk Ramsey ORCID: https://orcid.org/0000-0002-8641-9309

M Butzin ORCID: https://orcid.org/0000-0002-9275-7304

P Köhler ORCID: https://orcid.org/0000-0003-0904-8484

R Muscheler ORCID: https://orcid.org/0000-0003-2772-3631

P J Reimer ORCID: https://orcid.org/0000-0001-9238-2146

L Wacker ORCID: https://orcid.org/0000-0002-8215-2678

Abstract: Radiocarbon (^{14}C), due to its production in the atmosphere and subsequent dispersal through the carbon cycle, is a key tracer for studying the Earth system. Knowledge of past ^{14}C levels improves our understanding of climate processes, the Sun, the geodynamo, and the carbon cycle. Recently updated radiocarbon calibration curves (IntCal20, SHCal20, and Marine20) provide unprecedented accuracy in our estimates of ^{14}C levels back to the limit of the ^{14}C

technique (~55,000 years ago). Such improved detail creates new opportunities to probe the Earth and climate system more reliably and at finer-scale. We summarize the advances that have underpinned this revised set of radiocarbon calibration curves, survey the broad scientific landscape where additional detail on past ^{14}C provides insight, and identify open challenges for the future.

Radiocarbon (^{14}C) is most well-known for providing chronologies and age estimates via radiocarbon dating, a technique first developed by Willard Libby (*1*). However, its importance extends much further, allowing us to probe the fundamental relationships between multiple compartments of the Earth and climate system. It also provides a long-term perspective on past solar activity.

Excluding anthropogenic sources connected with nuclear research, industries and weapon testing after 1940, ^{14}C is predominantly produced in the upper atmosphere by a chain of reactions started by incoming galactic cosmic rays. The intensities of these rays, and hence ^{14}C production rates, are spatially and temporally modulated by the Sun and the Earth's magnetic field. Occasional significant additional ^{14}C production can also occur during extreme solar storms via highly energetic solar particles. After production, ^{14}C is oxidized to $^{14}CO_2$ and redistributed through the carbon cycle (Figure 1). Consequently, knowledge of past ^{14}C levels in the various oceanic and terrestrial carbon reservoirs helps to quantify processes in astrophysics, geophysics and biogeochemistry, with implications for climate science. This approach is enhanced when ^{14}C is considered alongside other cosmogenic nuclide records and recent advances in Earth system modeling.

This review focuses on pre-1950 levels of ^{14}C and their non-anthropogenic influences. We do not discuss the post-1950 bomb-spike in ^{14}C levels due to nuclear weapons testing (*2*) which provides insight into both carbon transport and biology (*3*). Similarly, we do not discuss in detail the dilution of atmospheric $^{14}CO_2$ caused by the burning of ^{14}C-free fossil fuel and cement production since the industrial revolution (*4*), the continuation of which will introduce future ambiguity in identifying the calendar ages of Holocene samples via radiocarbon dating (*5*). Regional measurement of this "Suess effect" allows estimation of local industrial CO_2 emissions (*3*).

Estimates of pre-1950 atmospheric and mean surface ocean ^{14}C levels are provided by the International Calibration (IntCal) Working Group who regularly collate ^{14}C measurements on samples of known, or independently estimated, calendar age from a range of archives including tree-rings, lacustrine and marine sediments, speleothems, and corals. These archives are assessed for quality-control and integrated to provide the IntCal set of calibration curves. The latest IntCal calibration curves, released in 2020, comprise IntCal20 for the Northern Hemisphere (NH) atmosphere (*6*), SHCal20 for the Southern Hemisphere (SH) atmosphere (*7*), and Marine20 (*8*) for the surface oceans.

Recent inter-disciplinary advances, including the ability to measure ^{14}C efficiently in very small samples such as single tree-rings (*9*), the availability of many new archives including those covering the last glacial period (*10*), and improved modeling (*8*, *11*, *12*) provide new levels of accuracy, precision, and detail in the IntCal20 curves when compared to the previous IntCal13 estimates (*13*, *14*). Consequently, there are new opportunities for using ^{14}C to study the behavior of both the Sun and the Earth's dynamo, undertake better absolute dating and synchronization of paleoclimate records, and obtain new insight into the carbon cycle and climate system.

When discussing ^{14}C, calendar ages are expressed as *cal BP* calendar years before present (defined as 1950 CE). $\Delta^{14}C$ denotes the (age-corrected) $^{14}C/^{12}C$ ratio, i.e. shows relative changes in the $^{14}C/^{12}C$ ratio, compared to a standard (*15*).

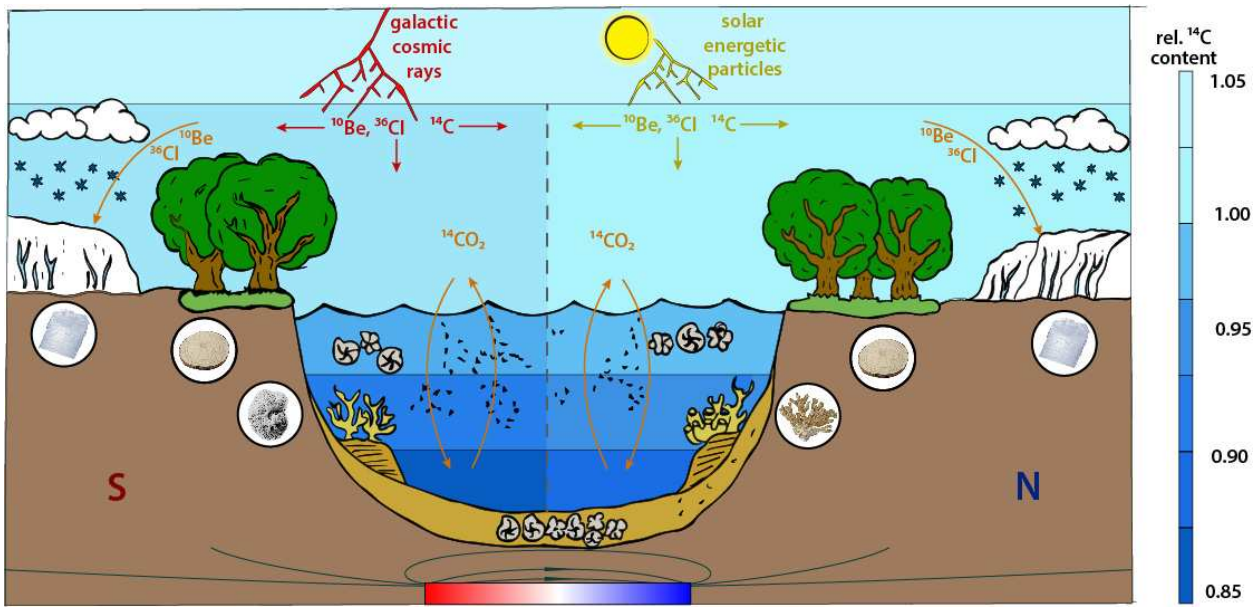

Figure 1 The production and subsequent distribution of ^{14}C and other cosmogenic radionuclides throughout the Earth system. *Production of ^{14}C and other cosmogenic nuclides (such as ^{10}Be and ^{36}Cl) occurs mainly in the stratosphere and upper layers of the troposphere driven by incoming galactic cosmic rays. While the galactic cosmic ray flux is assumed constant and isotropic, nuclide production rates are spatio-temporally modulated by magnetic shielding influenced by both the Sun's activity and the strength of the Earth's magnetic field. Further nuclide production can result from the release of solar energetic particles during extreme solar storms. After production, the nuclides are dispersed through the Earth system. In the case of ^{14}C, this dispersal occurs via the carbon cycle resulting in different ratios of ^{14}C, compared to stable ^{12}C, in its various oceanic and terrestrial compartments – the blue color scale shows the approximate $^{14}C/^{12}C$ ratios relative to the northern troposphere. Past levels of radionuclides are recorded in a range of archives. For ^{14}C these archives include tree-rings, stalagmites, corals, and lacustrine and marine sediments containing foraminifera; while ^{10}Be and ^{36}Cl are recorded in ice cores and sediments. Simultaneous comparison of ^{14}C levels in the different carbon cycle compartments, used alongside other cosmogenic nuclides, informs us about the climate system and carbon cycle processes over time, and provides insight into the Sun and the geodynamo.*

Recent Improvements in our Understanding of Past ^{14}C

Tree-rings: AMS evolution and annual resolution

The gold-standard for the reconstruction of past atmospheric ^{14}C levels are measurements of tree-ring sequences that have been independently dated using dendrochronology. The availability of new archives, as well as the higher capacity of new generation Accelerator Mass Spectrometry (AMS) (*16*, *17*), have enabled a rapid expansion in the availability of such data. We can now provide a precise estimate of NH atmospheric ^{14}C from 14,000 – 0 cal BP using solely tree-rings.

This estimate draws upon 9211 ^{14}C measurements on tree-rings of known age dated by either ring-width or isotope dendrochronology extending from 12,308 – 0 cal BP, and 1498 measurements on older tree-rings for which calendar ages are estimated based upon ^{14}C matching (*18–20*).

AMS has also enabled precise measurement of much smaller samples. Several grams of wood are needed for a high-precision ^{14}C measurement with older decay counting methods, typically limiting resolution to 10-year blocks. AMS is now able to provide similar precision but with only a few milligrams of material (*9*). This allows efficient and accurate measurement of ^{14}C in single growth-rings giving insight into short-term, annual, fluctuations in ^{14}C production (*21*).

Almost half (4952) the tree-ring ^{14}C measurements used to construct the IntCal20 NH estimate, covering 2731 individual calendar years, relate to determinations of single growth-rings. Particular examples where annual resolution ^{14}C data have provided significant insight include the sharp sudden spikes in ^{14}C production (Figure 2B) in e.g. 774-775 CE (*22*) and 993-994 CE (*23*) caused by extreme solar proton events (SPEs) (*24*); and the extension into the Younger Dryas (Figure 2C), a critical period of late-glacial climate change (*19*, *20*).

The number of laboratories providing reliable ^{14}C measurements has also increased, with 20 laboratories submitting data for the IntCal20 curves, reducing the previous reliance on datasets from single laboratories and associated dangers of systematic bias. The use of multiple laboratories has enabled inter-laboratory comparisons to improve the accuracy of ^{14}C measurements (*25*, *26*).

Extending the NH atmospheric ^{14}C estimates back to 55,000 cal BP

Further back in time, beyond 14,000 cal BP, insufficient tree-ring measurements exist to estimate the levels of ^{14}C precisely using these samples alone. Instead, we are reliant upon combining data from a wider range of archives. The backbone of the IntCal20 ^{14}C estimate in this older time period is provided by three stalagmites from Hulu Cave, China (*10*, *27*). These stalagmites provide a continuous ^{14}C record, consisting of measurements at over 400 unique calendar ages, extending from 54,000 – 13,900 cal BP. They provide new insight into ^{14}C levels before 30,000 cal BP, in particular around the Laschamps geomagnetic excursion (~41,000 cal BP, Figure 2A). These data are augmented by additional ^{14}C determinations from terrestrial macrofossils and foraminifera found in lake and ocean sediments, corals, and stalagmites from other locations (*6*).

We have also begun to find *floating* tree-ring sequences from before 14,000 cal BP for which relative internal ages are known by ring-counting but absolute ages are not (*28–30*). Radiocarbon measurements from these can be stitched-in alongside the other archives to add resolution and detail to the NH estimate, as well as enable assessment of modeling assumptions. In particular, three floating tree-ring sequences now cover the last deglaciation between 14,900 – 14,100 cal BP revealing previously unseen ^{14}C variations during this key warming period (*28*).

All these older data are more complicated since their calendar ages are not known precisely but instead are estimated. In the case of corals and stalagmites, these estimates are provided by Uranium-Thorium (U-Th) dating. Some of the sediment ^{14}C archives can be provided with a relative calendar-age chronology by layer-counting their annual varves (*31–33*). Other sediment

archives (*6*) are provided with calendar age estimates by tuning abrupt climate shifts seen in their various proxies to high-resolution $\delta^{18}O$ also recorded in the Hulu Cave stalagmites (*34*). Based on evidence for globally-synchronous timing of the selected rapid paleoclimatic changes (*35*), this allows transferal of calendar age information from Hulu Cave's U-Th timescale.

The necessity of including stalagmite and marine archives introduces further complexity since, unlike wood or terrestrial macrofossils in lake sediments, these archives do not record atmospheric ^{14}C directly. Stalagmites contain carbon from a range of sources including a "dead carbon fraction" from ancient limestone and soil carbon which is devoid or depleted of ^{14}C. Marine ^{14}C records are also depleted, compared to the contemporaneous atmosphere, due to the time it takes to exchange $^{14}CO_2$ at the ocean surface and mixing/exchange with "old" carbon from the ocean interior. To use these archives to construct an atmospheric ^{14}C record, this depletion must be adjusted for. The dead carbon fraction within a speleothem is estimated by comparing its ^{14}C depletion against ^{14}C from dendrochonologically-dated tree-rings, while marine depletion can be estimated by the same approach and computer modeling (*12*).

In total, the current IntCal20 estimate of NH ^{14}C from 55,000 – 14,000 cal BP period draws upon measurements from over 1900 unique calendar ages.

Combining the diverse ^{14}C archives to estimate the past NH atmospheric levels

The varied ^{14}C archives are carefully synthesized, recognizing their individual characteristics and potentially uncertain calendar ages, to provide a robust and reliable hemispheric-average estimate. A Bayesian spline regression approach is taken, incorporating expert prior information where available (*11*). This provides a set of complete posterior ^{14}C realizations, each representing a plausible ^{14}C history. These realizations allow access to covariance information on ^{14}C levels in adjacent years for use in subsequent modeling studies, or they can be summarized to provide pointwise estimates and probability intervals in any given year (Figure 2).

This approach to curve construction retains the critical detail and high-frequency variations, needed to unlock the full interrogative potential of ^{14}C, from the large volume of finely-resolved tree-ring data between 14,000 – 0 cal BP. However, from 55,000 – 14,000 cal BP only a coarser-scale estimate is possible due to the sparser and less direct nature of the diverse archives used, together with their uncertain calendar ages. Radiocarbon features seen within multiple archives are identified and maintained while ensuring individual outlying measurements, which may not provide an accurate atmospheric reconstruction, do not overly influence the estimate. Consequently, from 55,000 – 14,000 cal BP, a period containing key changes to both the carbon and climate systems, only the lower frequency components of the ^{14}C signal are identifiable. Higher frequency signals, which could be key to fully understanding the processes by which these changes occurred, cannot currently be resolved and await recovery of new archives through ongoing and future fieldwork.

Obtaining SH atmospheric and global surface-ocean ^{14}C estimates

2094 ^{14}C determinations are also available on SH tree-rings which enable the study of the variable North-South interhemispheric ^{14}C-gradient that is likely a result of the greater expanse of the oceans and higher air-sea CO_2 flux in the SH. However, less than 15% are determinations

of single growth-rings limiting our ability to identify small interhemispheric ^{14}C-gradient changes. Further, their calendar age coverage is uneven and independent estimates of atmospheric SH ^{14}C levels are only available in four distinct periods from 2140–0, 3520–3453, 3608–3590 and 13,140–11,375 cal BP (*20*). Outside these periods the interhemispheric ^{14}C-gradient is statistically modelled to construct a SH estimate extending from 55,000 – 0 cal BP (*7*).

A computer-model-based estimate for ^{14}C levels in the global-average surface ocean (*8*) has also been constructed. This is based on a Monte-Carlo ensemble of model runs driven by individual atmospheric IntCal20 ^{14}C realizations, CO_2 reconstructions from ice core records and prior estimates for both air-sea CO_2 exchange and ocean circulation. It simulates large-scale changes in ocean surface ^{14}C due to paleoclimatic and ^{14}C production rate changes, and enables users to distinguish regional ^{14}C ocean effects from variations due to such global changes (*36*).

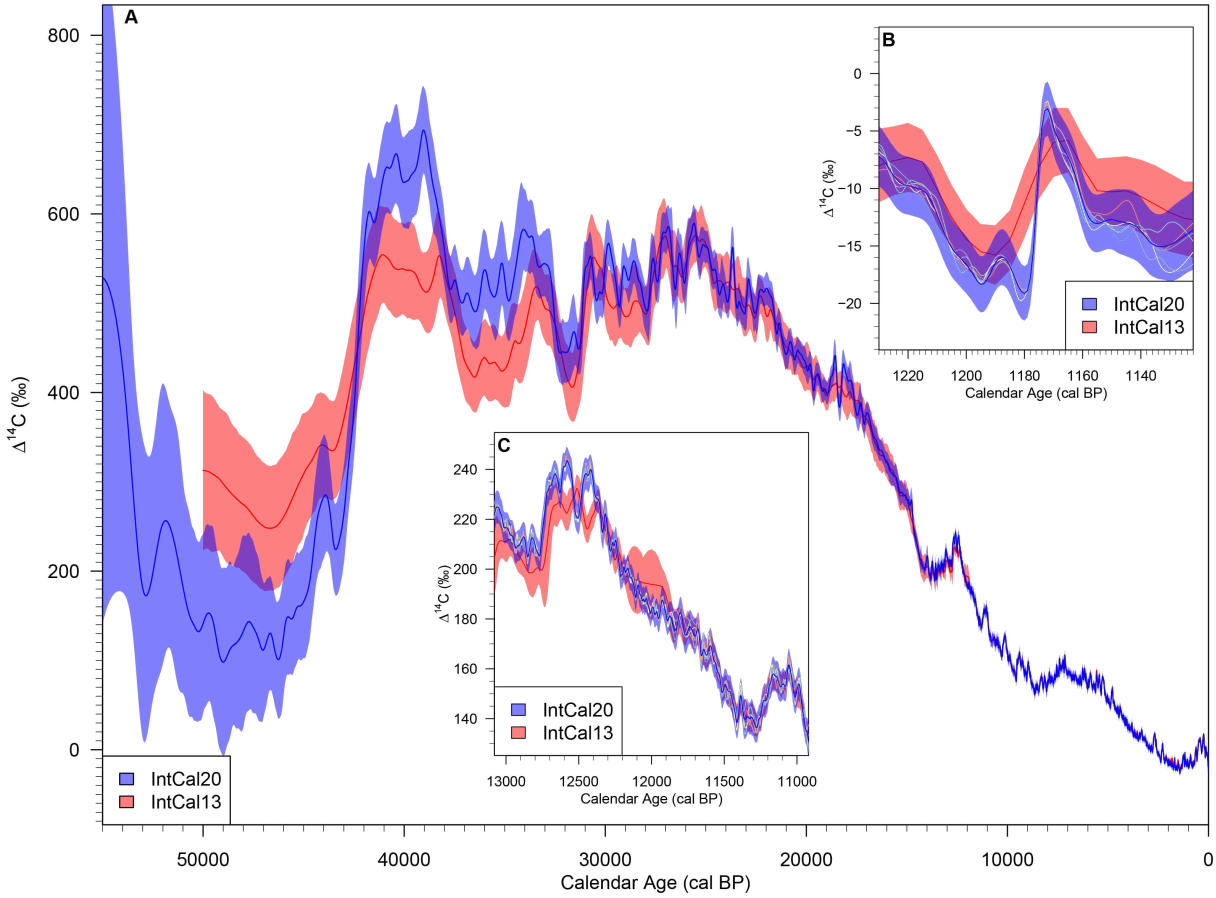

Figure 2 IntCal20 NH estimate of atmospheric ^{14}C variations (expressed as Δ^{14}C) over the last 55,000 years compared with the previous IntCal13 estimate*. The additional ^{14}C detail in the IntCal20 curve is due to the availability of new archives, combined with recent advances in measurement and modeling. Panel A: A plot of the posterior mean (solid line) and 2σ credible interval (shaded area) of the curves. Note in particular the significant increase in Δ^{14}C identified in IntCal20 around the Laschamps geomagnetic excursion (~41,000 cal BP) observed in Hulu Cave. Panel B: The 774-775 CE Event (1176 – 1175 cal BP) showing the sharp increase in Δ^{14}C*

identified with the annual data of IntCal20. This event was not observed in the lower resolution IntCal13. Shown are a sample of individual posterior IntCal20 curve realizations that enable a user to access covariance information (variously-colored lines); and the summarized posterior mean (solid blue line) and 2σ credible interval (shaded blue). Panel C: The extension of annually-resolved data into the Younger-Dryas provides a much more detailed ^{14}C estimate during a key period of climate change than was available with the IntCal13 curve. Individual IntCal20 curve realizations are plotted (variously-colored lines) together with the posterior IntCal13 and IntCal20 means and 2σ credible intervals.

Radiocarbon and the Sun

Changes in solar activity have the potential to generate significant impacts on Earth, notably on climate, while solar storms can cause serious harm to telecommunications, navigation systems, air and space travel, and electrical power grids.

Systematic solar activity measurements started in the early 17th century when observations of sunspots with telescopes began (*37*). For the last century, the sunspot record has been complemented with other instrumental records from ground-based observatories, space probes and satellites. However, these short-term instrumental records are insufficient for a complete understanding of the Sun, its magnetohydrodynamical behavior, and predictions on the full range of solar variability.

Cosmogenic radionuclide records, such as ^{14}C and ^{10}Be, provide the best "proxy" data for extending solar activity reconstructions beyond the period of instrumental measurements. Such extensions are needed to investigate longer-term solar variations and cycles that likely have most climatic significance (*38–41*).

Study of ^{14}C and other cosmogenic nuclides has also revealed massive past releases of solar particles in SPEs that exceed known solar storms of the instrumental era by an order of magnitude (*22–24*, *42*). If repeated today, such events have the potential to catastrophically damage current communications, power and satellite systems. Understanding the size and frequency of these huge solar storms is needed to mitigate their future risk. Radionuclide records provide the greatest potential to do so.

Probing Solar Cycles

During periods of high solar activity, a stronger solar magnetic shielding of galactic cosmic rays in the heliosphere leads to lower radionuclide production on Earth, and vice versa. This modulation of the radionuclide production rate by solar activity is well illustrated by comparison of radionuclide records and sunspot number observations over the past four centuries (Figure 3) and can be modelled quantitatively (*43*, *44*).

The geochemical behavior of radionuclides from production to deposition does however complicate their interpretation. Due to efficient mixing, atmospheric ^{14}C is not prone to large climatic impacts or weather noise on shorter (annual to decadal) time scales. However, atmospheric ^{14}C has the disadvantage that short-term variations due to the 11-yr solar cycle (*21*) are damped due to the carbon cycle (*45*). In contrast, the shorter atmospheric residence time of

^{10}Be and ^{36}Cl largely preserves their cyclic 11-yr variability in ice cores but weather and climate influences on the transport and deposition add noise. Further, the relative geomagnetic modulation of cosmogenic production is maximized at the equator, while the solar-induced production variation is maximized at the poles. Although most production occurs in the stratosphere characterized by intense horizontal mixing and relatively long residence time, any deviation from complete homogenous atmospheric mixing would affect the relative amplitudes of the geomagnetic and solar signals embedded in ^{10}Be and ^{36}Cl ice-core records.

Longer-term radionuclide records over the Holocene reveal additional cyclic changes with the most prominent being the 207-yr "de-Vries" and 88-yr "Gleissberg" cycles (*46*). Since ^{14}C and ^{10}Be records largely agree on these time scales (*47*) we can attribute common variation to production rate changes. Their solar origin is supported since there is no evidence of sufficiently large and rapid geomagnetic field changes to explain such centennial-scale cyclic changes. Further, the Maunder minimum, a 70 year-long period (1650 – 1715 CE) characterized by an almost complete lack of observable sunspots and coinciding with the middle of the Little Ice Age (*37*, *48*), can be regarded as one of the latest expressions of the de-Vries cycle (Figure 3).

Radiocarbon and ^{10}Be-based solar activity records allow reconstruction of solar irradiance variations used as inputs to global climate models alongside other natural (e.g. volcanic aerosols) and anthropogenic forcings (e.g. emissions of CO_2 and other greenhouse gases). The first attempt (*40*) was used for the IPCC AR4 report. These solar forcing curves have been improved through the use of complex models relating the ^{10}Be and ^{14}C records to solar irradiance to provide common inputs (*49*) for IPCC AR5 and AR6 climate models.

Radionuclides also suggest a possible bundling of periods of low solar activity with a quasi-periodicity of ~2000-2500 years and potentially significant effects on climate (*50*). However, very little is known about changes in solar activity with such long periodicities. Tree-ring ^{14}C records and ice-core ^{10}Be records do not agree well on time scales of 1000 years and longer, even after correcting for geomagnetic field influences and the different geochemical behavior (*47*). This could be a consequence of unknown carbon cycle effects on ^{14}C, climate effects on ^{10}Be transport and deposition, or uncertainties and biases within the paleomagnetic/archaeomagnetic reconstructions used to correct the ^{14}C and ^{10}Be signals. Until these effects are resolved, inference on solar activity changes on millennium time scales and longer remains speculative.

Higher resolution and better quality ^{14}C data offer great potential to improve studies on solar activity changes into the last ice age. This longer-term perspective might be crucial since memory effects due to the carbon cycle could affect atmospheric ^{14}C long into the Holocene (*51*) and bias solar activity reconstructions. In parallel, improvements in quality and resolution of ^{10}Be measurements in ice cores provide the opportunity to study solar cycles back several hundreds of thousands of years (*52*).

Massive Solar Proton Events

The Sun also generates solar cosmic rays – energetic particles emitted from active regions on the surface of the sun or accelerated in so-called coronal mass ejections. Study of solar storms during the instrumental period suggests that solar particles might increase the annual radionuclide

production rate by only a few percent (*53*), far too small to have an effect on the smoothed atmospheric ^{14}C levels or to be reliably detected in noisy ^{10}Be and ^{36}Cl records.

However, past ^{14}C records identify significant inter-annual spikes, most clearly during an event where atmospheric ^{14}C increased by 1.2% over the year 774 – 775 CE (*22*). Considering the smoothing effect of the carbon cycle this indicates a huge spike in ^{14}C production, generating almost four times the average yearly production. This cannot be explained by lower solar shielding of galactic cosmic rays. Co-occurring ^{10}Be and ^{36}Cl spikes in ice cores allow the robust attribution of this event to one or several successive massive SPEs (*24*).

Subsequent high-resolution studies of cosmogenic radionuclide records have enabled the identification of additional SPEs, e.g. 993 – 994 CE (*23*) and ~660 BCE (*42*), and a more detailed understanding of their nature (*54*). These SPEs do not just provide evidence of the Sun's potential to produce extreme events. Their unique global signature also offers the potential to precisely synchronize, to annual precision, climate records from tree-rings and ice cores (*55*).

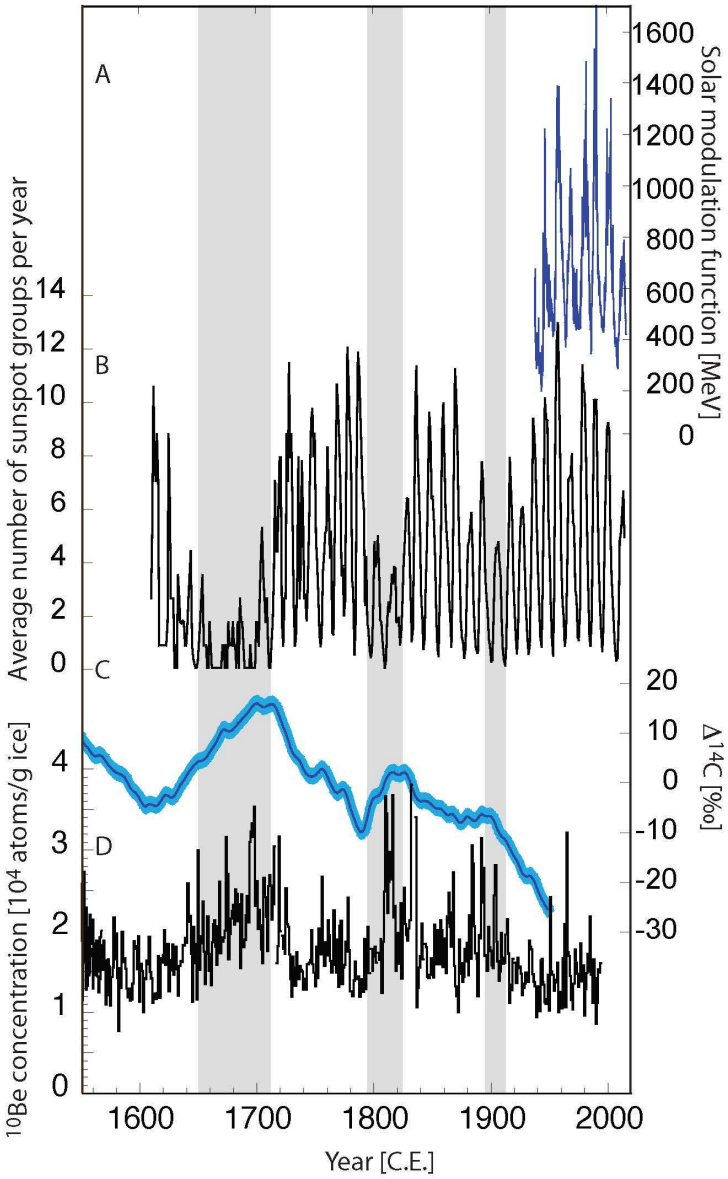

Figure 3 Direct and indirect data on past changes in solar activity. *Panel A: A reconstruction of the solar shielding of galactic cosmic rays based on neutron monitor measurements* (*56*). *Panel B: Group sunspot number reconstruction* (*48*). *Panel C: The IntCal20 NH $\Delta^{14}C$ estimate (mean ± 2σ)* (*6*). *It mirrors the ups and down in solar activity and shows the "^{14}C-Suess effect" i.e. the decrease of atmospheric ^{14}C in relation to the stable ^{12}C that began at the start of the industrial revolution in 1850 and is due to the massive release of ^{14}C-free CO_2 from the burning of fossil fuel* (*4*). *Panel D: Annual ^{10}Be data* (*57*) *shows significant weather noise but has a better potential to preserve the amplitude of the variations (±20%) connected to the 11-yr solar cycle and show the cycle's influence on the shielding of galactic cosmic rays. The grey bands show the period of the Maunder minimum around 1700, the Dalton minimum around 1800 and the shorter 1900 low solar activity period.*

Radiocarbon and the Geodynamo

The magnetic field observed at the Earth's surface is generated by turbulent convective flows of an electrically-conducting iron-nickel fluid in the Earth's outer core, a process known as the geodynamo. Since Gauss's first measurements in the mid-19th century, the intensity of the geomagnetic field has continuously decayed – it is now almost 10% weaker than in 1840 CE (*58*). This recent evolution is unexplained and must be considered in the context of longer-term geodynamics. Documenting temporal variations in the intensity of the geomagnetic field is fundamental for understanding the dynamics of the Earth's deep interior and the evolution of the Earth system.

Reconstructions of the past geomagnetic field intensity can be obtained from various archives. Thermoremanent magnetization of volcanic rocks and archaeological archives (e.g. baked clays) provides absolute field intensities (*59*, *60*) but represent sporadic recording of the local and instantaneous, rather than global dipolar, field.

By contrast, detrital remanent magnetization of marine and lacustrine sediments provides continuous records which average short-term deviations. However, sediments only provide a relative estimate of the geomagnetic field. They must be normalized and calibrated to the present-day dipole intensity or absolute values for past periods based on volcanic or archaeological archives (*61–63*). Further, the geomagnetic field is fossilized at some depth below the sediment-water interface (lock-in depth), leading to stratigraphic and dating uncertainties. Biases can also be introduced due to changes in the sediment composition, notably its magnetic mineral content.

Reconstructions of geomagnetic paleointensity over the past 100,000 years (*64*) using these two sets of archives are characterized by high-amplitude variations, most notably the Laschamps geomagnetic excursion (~41,000 cal BP) (*65*). However, these reconstructions exhibit large uncertainties hampering accurate estimation of the duration of excursions, the transitional trends into and out of excursions, and any rapid variations during the excursions themselves. These uncertainties hinder precise testing of magnetohydrodynamic models (*66*). Further progress is dependent upon both advances in numerical modeling and significant improvements to the paleomagnetic database.

Radiocarbon and other cosmogenic nuclides also provide constraints on geomagnetic field intensity variations via integration of their production rates over the whole Earth (*67*, *68*). Periods characterized by weak magnetic shielding lead to significant increases in nuclide production (*69–72*). The largest anomaly in the atmospheric $\Delta^{14}C$ record, from 42,000 – 39,000 cal BP (Figure 4), corresponds to the Laschamps geomagnetic excursion. This excursion also sees enhanced ^{10}Be and ^{36}Cl deposition in Antarctica and Greenland ice cores (*71*, *73*, *74*), and a prominent ^{10}Be peak in marine sediment records (*75*, *76*).

Although comparisons of ^{14}C, ^{10}Be and ^{36}Cl with paleomagnetic intensity records exhibit several correspondences, agreement remains far from optimal. Most notably, during the Laschamps geomagnetic excursion (Figure 4), the atmospheric $\Delta^{14}C$ rise between 46,000 – 41,000 cal BP is

ca. 600 ‰ (*6*), twice the amplitude predicted by paleomagnetic and cosmogenic radionuclide reconstructions (*10*, *63*, *77–79*). This suggests serious weaknesses in existing paleorecords or our understanding of the relationships between these geophysical and geochemical parameters.

A large discrepancy between different cosmogenic nuclides is also observed between 30,000 – 18,000 cal BP. Here, atmospheric $\Delta^{14}C$ stays above 400 ‰, while a polar ^{10}Be ice record and the mean of the geomagnetic reconstructions indicate a reduction in cosmogenic nuclide production rates that should have led to $\Delta^{14}C$ values lower than 200 ‰ (*77*). This discrepancy could be due to significant carbon cycle changes during the last glacial period (*69*, *71*, *77*, *80*). However, interpretation remains challenging due to the spread of paleomagnetic-based $\Delta^{14}C$ reconstructions (*77*). Additionally, ^{10}Be compiled from marine sediments (*75*, *81*) provides better agreement with ^{14}C leaving less room for a long-term impact of the carbon cycle (*82*).

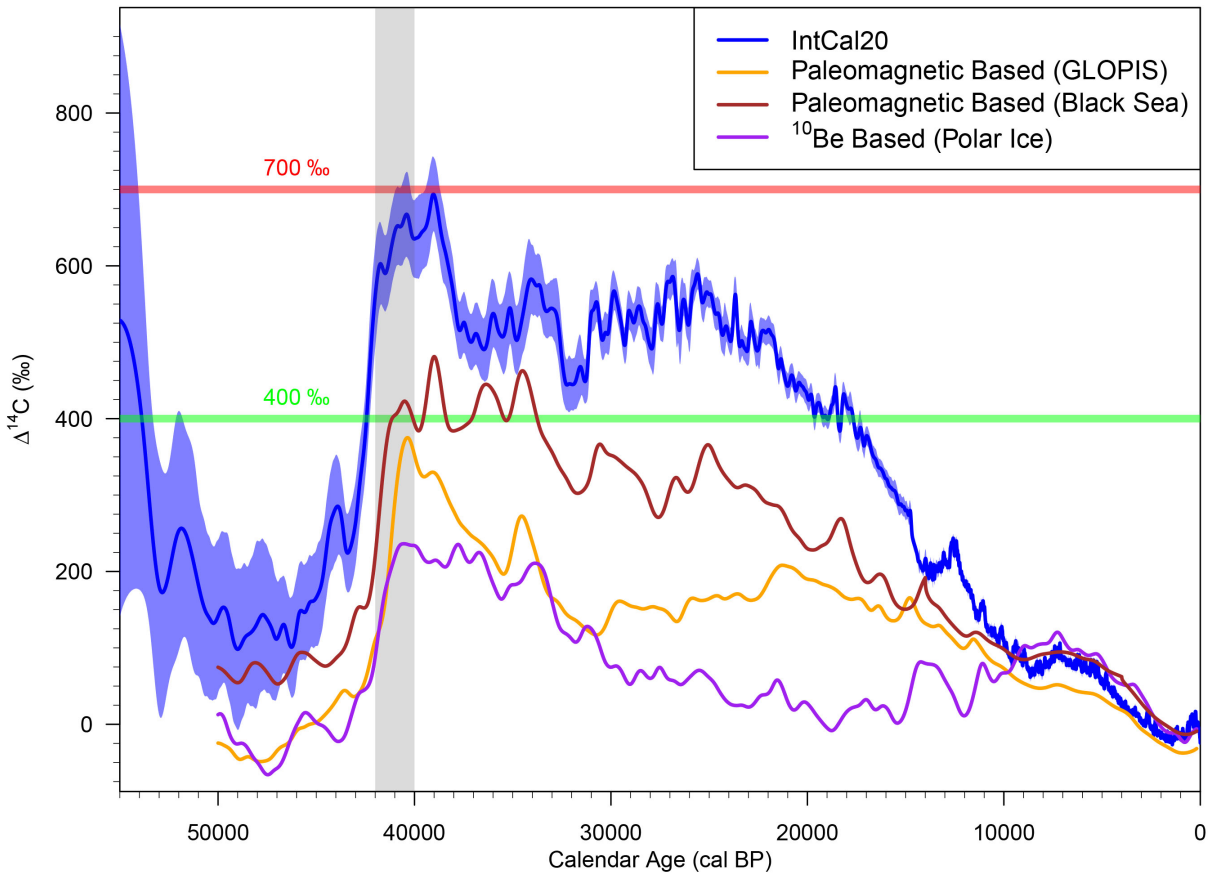

Figure 4 Comparison of the IntCal20 atmospheric $\Delta^{14}C$ estimate with paleomagnetic and cosmogenic radionuclide model-based reconstructions. *The measurement-based IntCal20 (blue) is shown alongside Bern3D model-based $\Delta^{14}C$ reconstructions for which ^{14}C production rates were calculated using geomagnetic field intensity (orange and brown) and ^{10}Be (purple) (77). Clear divergences between the IntCal20 estimate and the paleomagnetic- and ^{10}Be-based reconstructions are seen in the size of the atmospheric $\Delta^{14}C$ rise corresponding to the Laschamps geomagnetic excursion (shaded area from 42,000 – 40,000 cal BP). The differences extend to the beginning of the Holocene. The paleomagnetic reconstructions are based upon the Global Paleointensity Stack (GLOPIS) (78), and a high resolution combination of measurements*

from the Black Sea (63). The ^{10}Be reconstruction is based on a combination of radionuclide data from different ice cores including GRIP and GISP (79). All model-based reconstructions assume a constant preindustrial carbon cycle. Due to the wide spread of the various model-based reconstructions, it is not possible to conclude if the differences from the measurement-based IntCal20 atmospheric Δ^{14}C estimate are due to limitations and uncertainties in the paleomagnetic- and ^{10}Be -reconstructions of ^{14}C production rate, or a lack of knowledge in the ^{14}C cycle during the last glacial period.

Radiocarbon and Synchronization of Records

Study of past environmental changes is reliant on combining information from a range of records on diverse aspects of the Earth system. These include not only climate variables such as temperature and rainfall, but also information on plant, animal and human responses; habitat shifts; and long-term evolution. Each different record has its particular strengths but to use them optimally, they must first be placed on a timescale. However, various different timescales exist and the resultant chronological uncertainties can be considerable. This limits inference when multiple records need to be compared.

There is always the temptation to assume that changes seen in different records are synchronous, but this risks circularity if we are interested in possible leads and lags in the Earth and climate system that could inform on processes of change (*83*). We therefore need methods of comparing records which depend on variables that we have good reason to consider globally synchronous.

Particularly key for study of the last 55,000 cal BP are the ^{14}C-based timescale and the various ice-core chronologies. The common stratospheric production of cosmogenic isotopes provides a very powerful method for their synchronization. For both ^{14}C and ^{10}Be, while production is greatest near the poles, intense horizontal mixing and relatively long residence times (*84*) mean that changes in production rates, including annual spikes from SPEs, will be visible in the ^{14}C record of both hemispheres and ^{10}Be deposited in ice cores in both polar regions.

As explained previously, although the two nuclides cannot be compared directly (Figure 3) we can model variations in ^{14}C levels from the production rate variations seen in ^{10}Be. Matching common structure in the ^{10}Be and ^{14}C signals makes synchronization of ^{14}C-based chronologies with the ice core timescales possible. During the Holocene, where high resolution dendrochronologically-dated ^{14}C measurements are available, it is possible to pick up very fine structure and obtain synchronization with uncertainties of just a few years (*85*); while for SPEs annual precision is achievable (*55*). For earlier periods, synchronization is limited to larger, more significant excursions in the signal due to potentially confounding effects of carbon cycle changes, dating uncertainties, and lower data quality and resolution. Here, synchronization is also more uncertain and precision is closer to being centennial (*79*).

Both the radiocarbon and ice-core chronologies have their strengths: ice cores have very good internal relative precision in terms of the time-gaps between succeeding events; the ^{14}C-based timescale has more precise absolute age control through both dendrochronology and U-Th dating methods. For this reason, neither timescale is presently used to correct the other, but rather a

time-transfer function is used to convert one to the other, with associated uncertainties (*79*, *85*, *86*).

Given the methods used for construction of the radiocarbon calibration curves (see earlier), the fundamental timescale underlying calibrated radiocarbon dates is dendrochronology from 14,000 – 0 cal BP, and prior to 14,000 cal BP is largely based upon the highest resolution and accuracy provided by the U-Th chronology of the Hulu Cave speleothems (*10*, *27*).

Radiocarbon calibration, potentially in combination with deposition modeling (*87–89*), enables further environmental records to be synchronized onto this same ^{14}C-based timescale. With new high-resolution ^{14}C data, it is possible to get calibrated chronologies for tree-ring series approaching annual resolution, especially in those places where we have abrupt signals from SPEs. More typically, for records such as sedimentary deposits, decadal to centennial scale resolution is possible, except in the case of marine sediments where uncertainties in marine reservoir effects often limit our ability to synchronize records on the basis of radiocarbon alone.

Through combined use of ^{14}C and ^{10}Be, it is possible to construct a synchronization framework to cover a broad range of environmental and archaeological records spanning the last 55,000 cal BP (Figure 5). This framework can be further enhanced with other methods. Between ice cores, the annual counting chronologies can be tied together using volcanic stratigraphic markers such as volcanic ash shards (tephra) or sulfur maxima (*55*, *90–96*). Analysis of trace quantities of CH_4, another global signal, trapped within the ice (*97*, *98*) allows further synchronization of these ice-core chronologies. On a coarser scale, geomagnetic excursions such as the Laschamps allow linkages to longer Quaternary chronologies such as U-Th-dated speleothems (*10*, *79*). However, these other synchronization techniques are limited to very specific time periods. The keystone of the framework remains the ^{14}C-based timescale which provides the continuous metric on which we can study changes over the Holocene and much of the last glacial period.

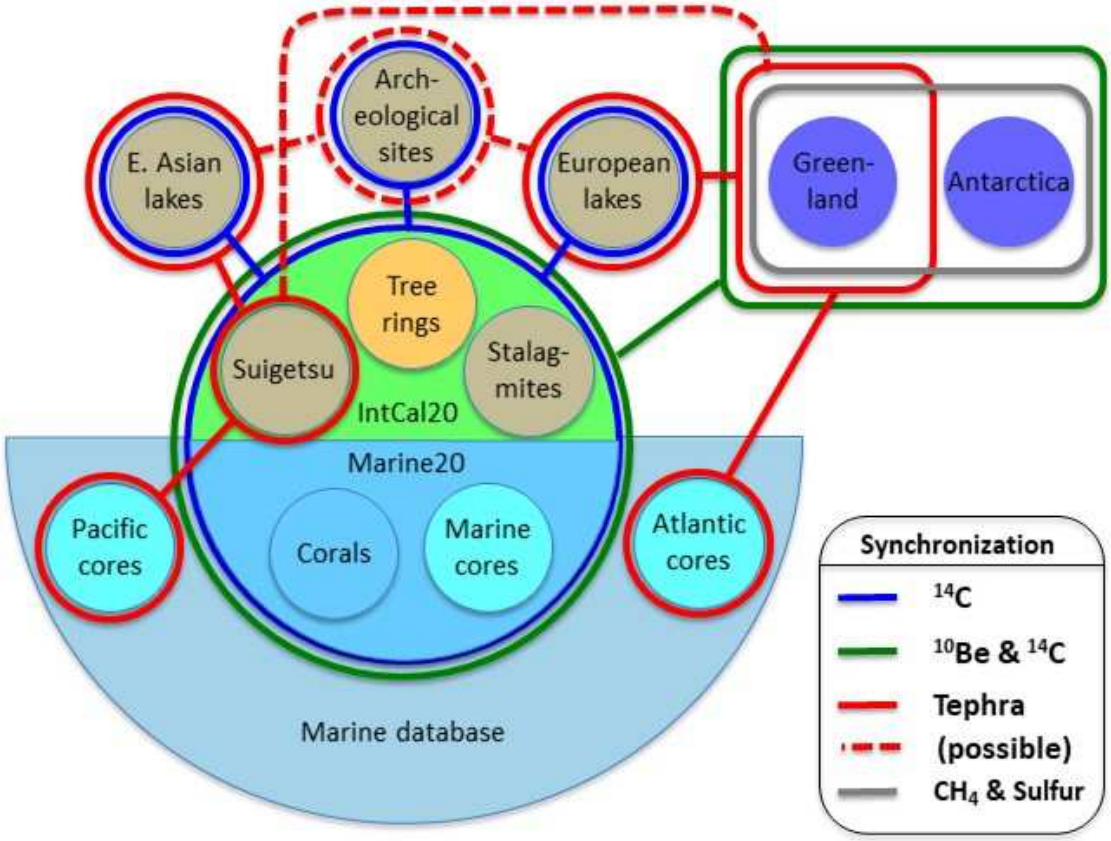

Figure 5 Schematic of the direct synchronization methods for records spanning the last 55,000 years. *These synchronization methods can be used to enhance or replace climate-based tuning of chronologies. The central circle shows the records contained within the IntCal20 dataset and directly synchronized through the statistical processes involved in the compilation using ^{14}C. Radiocarbon is also the primary method for relating terrestrial environmental and archaeological records to the primary IntCal ^{14}C-based timescale. Variation in marine offsets means that other methods such as volcanic ash shards (tephra) and other event-based methods are normally used to synchronize marine records. The link to ice-core chronologies is provided by looking at the relationship between ^{10}Be and ^{14}C, while between ice cores we can use a combination of local events and global signals, in particular CH_4, sulfur maxima, and ^{10}Be. Volcanic tephra layers provide a check and give precise synchronization at specific points in the chronology: these can be found in sedimentary records, ice cores, and some archaeological sites.*

Radiocarbon and the Carbon Cycle

The global carbon cycle plays a crucial role in our climate system. Changes to the carbon cycle affect the concentration of atmospheric CO_2, a key greenhouse gas and the main driver of current climate change. Since 1850 CE, the carbon cycle has removed nearly 60% of the anthropogenic

CO_2 emissions from the atmosphere and stored them away in the ocean and terrestrial biosphere reservoirs (*99*). Understanding the potential for responses and feedbacks of the carbon cycle, and consequently changes to this CO_2 sequestration, is therefore critical for future climate projections.

Past changes to the carbon cycle are however far from completely understood. While ice-core-based atmospheric CO_2 reconstructions (*100*) are available, the changes they show await detailed explanations. Since ^{14}C is dispersed via the carbon cycle after production, it can act as a unique tracer to help investigate.

On the 55,000 – 0 cal BP timescale relevant to ^{14}C, the dominant roles in the carbon cycle are played by the ocean (with pre-industrial stores of ~37,000 petagrams of carbon (PgC, 10^{15} gC)); the atmosphere (with ~280 ppm of CO_2 or ~600 PgC); and the land carbon cycle (~4,000 PgC) (*101*). Land carbon consists of active carbon (~2400 PgC) and inert carbon bound in permafrost soil (~1600 PgC). While small compared with the ocean stores, the role of this land carbon in determining atmospheric CO_2 cannot be neglected. From the last glacial maximum to the preindustrial, active carbon stores have increased while inert carbon stores have decreased (*101*), resulting in a net increase in land carbon of between 450 – 1250 PgC (*102*).

The carbon cycle's reservoirs are characterized by different $^{14}C/^{12}C$ ratios related to their respective carbon exchange with the atmosphere. In measuring the ^{14}C content of fossil samples characterizing these reservoirs we can reconstruct past carbon cycle changes. The interhemispheric ^{14}C-gradient can be studied by comparing ^{14}C in subfossil trees collected in both hemispheres. Further, planktonic and benthic foraminifera, surface corals and deep-water corals allow reconstructions of ^{14}C gradients at different depths and locations of the world ocean. Probing ^{14}C in terrestrial organic matter is more challenging due to the lack of large-scale exchanges between reservoirs and the intense mixing of carbon of different ages at local scale (e.g. in soils) (*103*).

Benthic-planktonic and benthic-atmospheric ^{14}C differences have been used to constrain changes in mean ocean circulation. Recent research estimated an increase of about 700 ^{14}C years in the average residence time of deep ocean carbon at the last glacial maximum compared to the preindustrial, suggesting much of the reduction in atmospheric CO_2 levels seen in this glacial period may have been due to greater carbon storage in the mid-depth Pacific (*104*). However, some glacial marine ^{14}C levels are so low that they suggest local influx of ^{14}C-depleted hydrothermal CO_2 at particular sites (*105*, *106*). Our understanding of highly-depleted deep-ocean ^{14}C data is therefore far from complete, requiring more data and the combination of climate and process-based solid Earth models (*107*).

Most abrupt carbon cycle changes are identifiable by jumps in atmospheric CO_2. Across the last deglaciation, three events (~16,500, 14,600, and 11,500 cal BP) have been detected where CO_2 rose by more than 10ppm in 1 – 2 centuries (*108*). CO_2 behavior also changed at the onset of the Younger Dryas (~12,900 cal BP) when levels began to consistently increase after more than 1500 years of relative stability.

Marine data and box-model simulations attribute most centennial- and millennial-scale CO_2 changes in the last 70,000 years to ocean circulation, specifically invigoration or weakening of

the Atlantic meridional ocean circulation and associated northward and southward shifts of the intertropical convergence zone (*109*, *110*). Radiocarbon can shed further light on this. Recent ^{14}C data suggest significant changes in the ^{14}C-interhemispheric gradient at the onset of the Younger Dryas (*20*) and reduced North Atlantic Deep Water formation rates (*36*). These temporal interhemispheric ^{14}C-gradient changes and proposed ocean circulation changes need further understanding with high-resolution Earth system modeling.

The NH permafrost area halved across the last deglaciation (*111*), implying a massive permafrost thawing and related carbon release detectable by permafrost-specific biomarkers in marine sediment cores bathed in runoff waters (*112–117*). Using ^{14}C, the pre-depositional age of the permafrost carbon can be determined, helping constrain site-specific climate conditions in the catchment areas.

Arctic permafrost thaw, due to sea-level rise, has been suggested as potentially responsible for the abrupt CO_2 jumps around 14,600 cal BP at the onset of the NH Bølling warming, and at 11,500 cal BP. As such thaw would have released large amounts of old (^{14}C-depleted) carbon, the contribution of permafrost can potentially be constrained by changes in atmospheric ^{14}C levels (*113*, *118*). These two CO_2 jumps are accompanied by synchronous rapid jumps in methane. Since ^{14}C measured in methane extracted from ice cores indicates no substantial methane releases from old carbon sources (*119*) it is possible that permafrost thaw may not be the only contributory process.

More detailed inference on climate changes to the ocean reservoir of the carbon cycle is available through ocean circulation models. This is possible since the deep-sea ocean circulation timescale coincides with the ^{14}C half-life. Typically, these models prescribe atmospheric ^{14}C levels and focus on understanding its ocean dispersal, specifically the levels of oceanic ^{14}C depletion. This depletion is location and time specific, and not only influenced by ocean circulation (Figure 6). Variations in wind stress and sea-ice cover cause significant spatio-temporal differences in air-sea $^{14}CO_2$ exchange (*120*, *121*). Glacial-interglacial variation in atmospheric partial pressure of CO_2 further affects this exchange (*121*, *122*), while turbulent mixing within the ocean may also introduce ^{14}C variations in the deep-sea unrelated to ocean circulation changes (*123*).

Modern-day ^{14}C measurements on sea-water have been the primary means used to assess these ocean circulation models (*124*). However, incorporation of further constraints provided by marine ^{14}C paleorecords holds promise to improve our understanding of the ocean's role in climate change and its response to rising atmospheric CO_2 (*120*, *125*). Unfortunately, this is complicated by the lack of resolution, amongst those global models which can run long-term simulations, near the ocean margins that provide the majority of ^{14}C paleorecords (*126*, *127*). Global multiresolution models may provide a solution (*128*), ideally coupled with models of all other carbon cycle components.

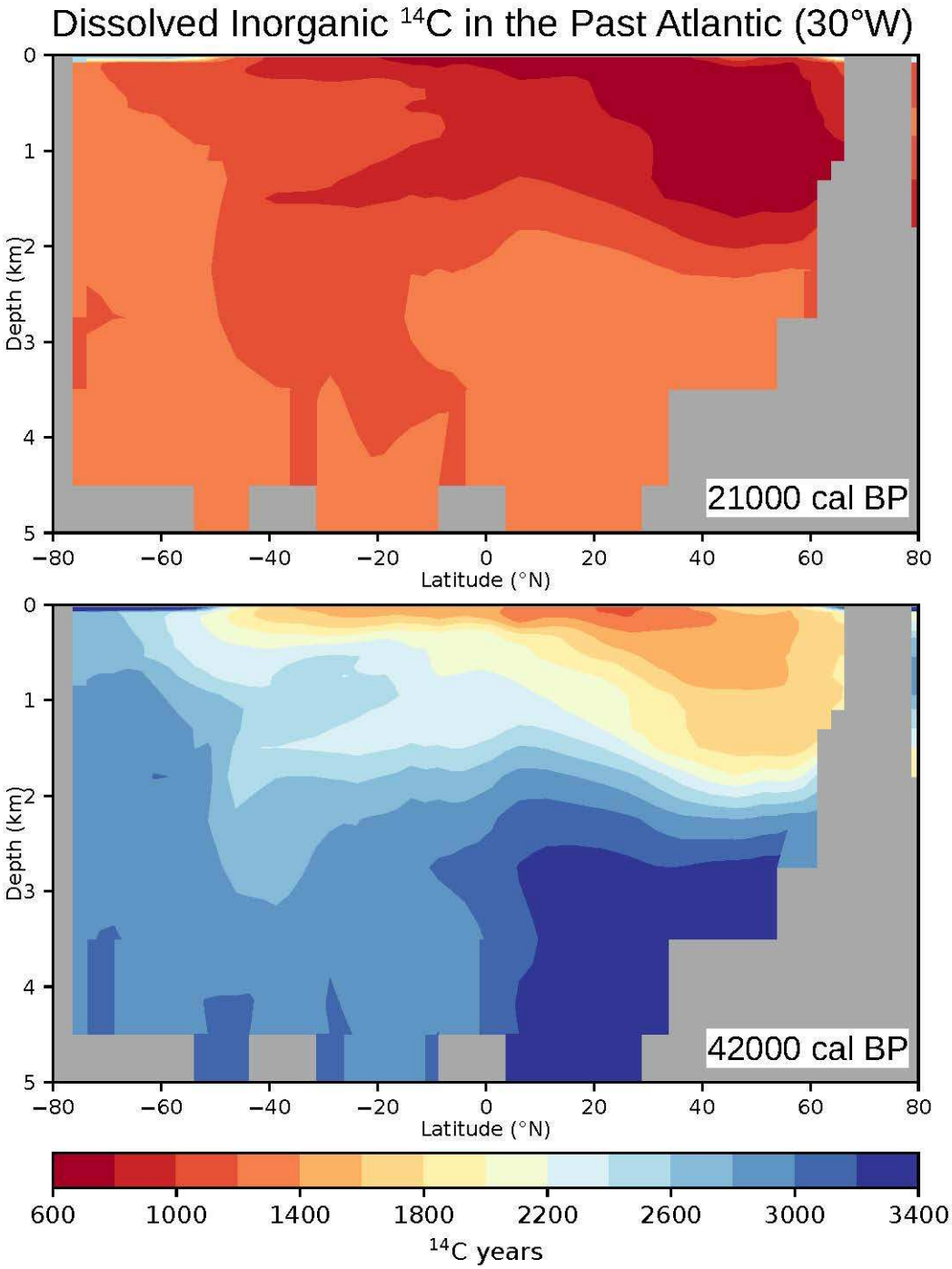

Figure 6 Radiocarbon distributions in the past Atlantic. *Depletion of dissolved ^{14}C with respect to the contemporaneous atmosphere for meridional sections along 30°W at 21,000 cal BP (around the Last Glacial Maximum, top) and 42,000 cal BP (the onset of the Laschamps geomagnetic excursion, bottom) according to an ocean general circulation model (12, 126). This model was run from 55,000 cal BP to 0 cal BP, forced with IntCal20 atmospheric $\Delta^{14}C$ and ice core CO_2 (6). Each panel displays the median of nine simulations. Depletion is expressed in terms of ^{14}C age. Low ^{14}C concentrations translate to high ^{14}C ages and vice versa. In both*

panels the average ocean circulation is the same. The differences between 21,000 cal BP and 42,000 cal BP are instead due to changes in atmospheric $\Delta^{14}C$ levels in combination with different leads and lags between these atmospheric $\Delta^{14}C$ changes and their oceanic uptake and dispersal.

Future Work

Despite the developments in our understanding and use of ^{14}C, considerable work still remains if we wish to harness its full potential as a tracer. This requires improvements to cosmogenic isotopic and paleomagnetic records, as well as improved modeling techniques.

Improving our ^{14}C estimates

Annual resolution NH ^{14}C measurements are currently only available on less than 20% of the timescale back to 14,000 cal BP and in some periods underlying data remain sparse. A coordinated approach to address this is needed since extending annual resolution tree-ring ^{14}C data would allow much longer-term research into past solar activity. Further, this would enable inference on the frequency and size of SPEs and potentially provide a wider set of markers on which to precisely synchronize ^{14}C and ice core records. Annual resolution extensions to the SH ^{14}C data sets would also help to better understand the interhemispheric ^{14}C-gradient and constrain past air-sea CO_2 fluxes.

Additionally, open questions remain on potential intra-hemispheric offsets in ^{14}C due to differences in growing season, species, altitude, latitude, or location of the recording tree-rings. Currently, deconvolution of these potential intra-hemispheric influences is confounded by inter-laboratory differences which are typically of similar scale to any potential offsets (*18*). The current NH ^{14}C record is predominantly reliant upon trees from European oak and pine. An extension to other tree-ring records would be aided via development of a broader set of dendrochronologically-dated tree-rings.

Most critically, we require a truly atmospheric ^{14}C record extending back to 55,000 cal BP that also provides sufficient detail to reliably and precisely reconstruct the high-frequency component of the ^{14}C signal. Extending annual resolution ^{14}C records back before 14,000 cal BP would provide new information on Earth system processes in a very different climate regime. Further it would enable ^{14}C records that arise from different compartments of the carbon cycle, in particular the marine environment, to be used independently. This would improve our predictions and understanding of climate and carbon cycle changes through enhanced validation of relevant models.

Potential sources of such terrestrial ^{14}C data include further macrofossil archives to add to those from Lake Suigetsu (*33*), and ideally the discovery of further floating tree-ring sequences. Both of these sources would however likely be complicated by the need to estimate their calendar ages. The most immediate hope for an extension perhaps lies in subfossil New Zealand kauri (*Agathis australis*) logs which have been found to cover much of the ^{14}C range, including the

Laschamps geomagnetic excursion (*129*). While only providing information on SH ^{14}C levels, such logs would still provide unprecedented precision and resolution.

Improvements to Other Records and Models

Extensions of ^{10}Be and ^{36}Cl records to a wider range of archives would be valuable - in particular new polar ice cores, but also less used archives such as marine and lacustrine sediments, low-latitude glacier ice cores, and packrat middens (*130*). Special emphasis should be made to better understand the relationships between production signal, atmospheric transport and deposition, and the ^{10}Be and ^{36}Cl concentrations in these archives.

Radionuclide records obtained at different latitudes, combined with numerical modeling of their production and spread in the atmosphere, would enable checks that ^{10}Be and ^{36}Cl records provide an accurate picture of the global solar and geomagnetic modulation.

Work is required to resolve remaining differences and uncertainties in the relationships between the geomagnetic and heliomagnetic fields and absolute production rates of ^{14}C, ^{10}Be and ^{36}Cl. These may be due to uncertainties in the galactic cosmic ray flux outside the heliosphere and the production cross sections for cosmogenic radionuclides.

Turning to the geodynamo, research is needed to improve databases on volcanic rocks and sediments, and to correct for the effects of non-dipolar components and various sources of blurring of individual paleomagnetic records (bioturbation, variable lock-in depth). Further, many paleomagnetic records based on marine sediments are not precisely dated, which could introduce biases when they are combined/stacked to estimate global geodynamo changes.

Improvements in carbon cycle modeling are also needed to better understand the differences that currently exist between measurement-based atmospheric $\Delta^{14}C$ estimates and model-based reconstructions using ^{14}C production rates obtained from ^{10}Be and paleomagnetic records.

Combined, such advances would provide a step-change in our ability to separate the geomagnetic, solar and carbon cycle components of the ^{14}C record. This would potentially permit detection of short-term geomagnetic events, and the resolution of hypothesized long-term trends in solar activity and changes in the carbon cycle.

References and Notes:

1. W. F. Libby, E. C. Anderson, J. R. Arnold, Age Determination by Radiocarbon Content: World-Wide Assay of Natural Radiocarbon. *Science*. **109**, 227–228 (1949).
2. Q. Hua, M. Barbetti, A. Z. Rakowski, Atmospheric Radiocarbon for the Period 1950–2010. *Radiocarbon*. **55**, 2059–2072 (2013).
3. H. Graven, R. F. Keeling, J. Rogelj, Changes to Carbon Isotopes in Atmospheric CO_2 Over the Industrial Era and Into the Future. *Global Biogeochem. Cycles*. **34** (2020), doi:https://doi.org/10.1029/2019GB006170.

4. H. E. Suess, Radiocarbon Concentration in Modern Wood. *Science*. **122**, 415–417 (1955).

5. P. Köhler, Using the Suess effect on the stable carbon isotope to distinguish the future from the past in radiocarbon. *Environ. Res. Lett.* **11**, 124016 (2016).

6. P. J. Reimer, W. E. N. Austin, E. Bard, A. Bayliss, P. G. Blackwell, C. Bronk Ramsey, *et al.*, The IntCal20 Northern Hemisphere Radiocarbon Age Calibration Curve (0–55 cal kBP). *Radiocarbon*. **62**, 725–757 (2020).

7. A. G. Hogg, T. J. Heaton, Q. Hua, J. G. Palmer, C. S. M. Turney, J. Southon, *et al.*, SHCal20 Southern Hemisphere Calibration, 0–55,000 Years cal BP. *Radiocarbon*. **62**, 759–778 (2020).

8. T. J. Heaton, P. Köhler, M. Butzin, E. Bard, R. W. Reimer, W. E. N. Austin, *et al.*, Marine20—The Marine Radiocarbon Age Calibration Curve (0–55,000 cal BP). *Radiocarbon*. **62**, 779–820 (2020).

9. L. Wacker, M. Němec, J. Bourquin, A revolutionary graphitisation system: Fully automated, compact and simple. *Nucl. Instruments Methods Phys. Res. Sect. B Beam Interact. with Mater. Atoms*. **268**, 931–934 (2010).

10. H. Cheng, R. L. Edwards, J. Southon, K. Matsumoto, J. M. Feinberg, A. Sinha, *et al.*, Atmospheric $^{14}C/^{12}C$ changes during the last glacial period from Hulu Cave. *Science*. **362**, 1293–1297 (2018).

11. T. J. Heaton, M. Blaauw, P. G. Blackwell, C. Bronk Ramsey, P. J. Reimer, E. M. Scott, The IntCal20 Approach to Radiocarbon Calibration Curve Construction: A New Methodology Using Bayesian Splines and Errors-in-Variables. *Radiocarbon*. **62**, 821–863 (2020).

12. M. Butzin, T. J. Heaton, P. Köhler, G. Lohmann, A Short Note on Marine Reservoir Age Simulations Used in IntCal20. *Radiocarbon*. **62**, 865–871 (2020).

13. P. J. Reimer, E. Bard, A. Bayliss, J. W. Beck, P. G. Blackwell, C. Bronk Ramsey, *et al.*, IntCal13 and Marine13 radiocarbon age calibration curves 0-50,000 years cal BP. *Radiocarbon*. **55**, 1869–1887 (2013).

14. A. G. Hogg, Q. Hua, P. G. Blackwell, M. Niu, C. E. Buck, T. P. Guilderson, *et al.*, SHCal13 Southern Hemisphere calibration, 0-50,000 years cal BP. *Radiocarbon*. **55** (2013), doi:10.2458/azu_js_rc.55.16783.

15. M. Stuiver, H. A. Polach, Discussion Reporting of ^{14}C Data. *Radiocarbon*. **19**, 355–363 (1977).

16. M. Suter, R. Huber, S. A. W. Jacob, H.-A. Synal, J. B. Schroeder, A new small accelerator for radiocarbon dating. *AIP Conf. Proc.* **475**, 665–667 (1999).

17. H.-A. Synal, M. Stocker, M. Suter, MICADAS: A new compact radiocarbon AMS system. *Nucl. Instruments Methods Phys. Res. Sect. B Beam Interact. with Mater. Atoms*. **259**, 7–13 (2007).

18. A. Bayliss, P. Marshall, M. W. Dee, M. Friedrich, T. J. Heaton, L. Wacker, IntCal20 Tree Rings: An Archaeological Swot Analysis. *Radiocarbon*. **62**, 1045–1078 (2020).

19. F. Reinig, A. Sookdeo, J. Esper, M. Friedrich, G. Guidobaldi, G. Helle, *et al.*, Illuminating

Intcal During the Younger Dryas. *Radiocarbon*. **62**, 883–889 (2020).

20. M. Capano, C. Miramont, L. Shindo, F. Guibal, C. Marschal, B. Kromer, *et al.*, Onset of the Younger Dryas Recorded with ^{14}C at Annual Resolution in French Subfossil Trees. *Radiocarbon*. **62**, 901–918 (2020).
21. N. Brehm, A. Bayliss, M. Christl, H.-A. Synal, F. Adolphi, J. Beer, *et al.*, Eleven-year solar cycles over the last millennium revealed by radiocarbon in tree rings. *Nat. Geosci.* **14**, 10–15 (2021).
22. F. Miyake, K. Nagaya, K. Masuda, T. Nakamura, A signature of cosmic-ray increase in AD 774–775 from tree rings in Japan. *Nature*. **486**, 240–242 (2012).
23. F. Miyake, K. Masuda, T. Nakamura, Another rapid event in the carbon-14 content of tree rings. *Nat. Commun.* **4**, 1748 (2013).
24. F. Mekhaldi, R. Muscheler, F. Adolphi, A. Aldahan, J. Beer, J. R. McConnell, *et al.*, Multiradionuclide evidence for the solar origin of the cosmic-ray events of AD 774/5 and 993/4. *Nat. Commun.* **6**, 8611 (2015).
25. L. Wacker, E. M. Scott, A. Bayliss, D. Brown, E. Bard, S. Bollhalder, *et al.*, Findings from an in-Depth Annual Tree-Ring Radiocarbon Intercomparison. *Radiocarbon*. **62**, 873–882 (2020).
26. E. M. Scott, P. Naysmith, G. T. Cook, Should Archaeologists Care about ^{14}C Intercomparisons? Why? A Summary Report on SIRI. *Radiocarbon*. **59**, 1589–1596 (2017).
27. J. Southon, A. L. Noronha, H. Cheng, R. L. Edwards, Y. Wang, A high-resolution record of atmospheric ^{14}C based on Hulu Cave speleothem H82. *Quat. Sci. Rev.* **33**, 32–41 (2012).
28. F. Adolphi, R. Muscheler, M. Friedrich, D. Güttler, L. Wacker, S. Talamo, *et al.*, Radiocarbon calibration uncertainties during the last deglaciation: Insights from new floating tree-ring chronologies. *Quat. Sci. Rev.* **170**, 98–108 (2017).
29. C. S. M. Turney, L. K. Fifield, A. G. Hogg, J. G. Palmer, K. Hughen, M. G. L. Baillie, *et al.*, The potential of New Zealand kauri (Agathis australis) for testing the synchronicity of abrupt climate change during the Last Glacial Interval (60,000–11,700 years ago). *Quat. Sci. Rev.* **29**, 3677–3682 (2010).
30. C. S. M. Turney, J. Palmer, C. Bronk Ramsey, F. Adolphi, R. Muscheler, K. A. Hughen, *et al.*, High-precision dating and correlation of ice, marine and terrestrial sequences spanning Heinrich Event 3: Testing mechanisms of interhemispheric change using New Zealand ancient kauri (Agathis australis). *Quat. Sci. Rev.* **137**, 126–134 (2016).
31. K. A. Hughen, J. R. Southon, C. J. H. Bertrand, B. Frantz, P. Zermeño, Cariaco Basin Calibration Update: Revisions to Calendar and ^{14}C Chronologies for Core Pl07-58Pc. *Radiocarbon*. **46**, 1161–1187 (2004).
32. C. Bronk Ramsey, T. J. Heaton, G. Schlolaut, R. A. Staff, C. L. Bryant, A. Brauer, *et al.*, Reanalysis of the Atmospheric Radiocarbon Calibration Record from Lake Suigetsu, Japan. *Radiocarbon*. **62**, 989–999 (2020).

33. C. Bronk Ramsey, R. A. Staff, C. L. Bryant, F. Brock, H. Kitagawa, J. van der Plicht, *et al.*, A Complete Terrestrial Radiocarbon Record for 11.2 to 52.8 kyr B.P. *Science*. **338**, 370–374 (2012).

34. H. Cheng, R. L. Edwards, A. Sinha, C. Spötl, L. Yi, S. Chen, *et al.*, The Asian monsoon over the past 640,000 years and ice age terminations. *Nature*. **534**, 640–646 (2016).

35. E. C. Corrick, R. N. Drysdale, J. C. Hellstrom, E. Capron, S. O. Rasmussen, X. Zhang, *et al.*, Synchronous timing of abrupt climate changes during the last glacial period. *Science*. **369**, 963–969 (2020).

36. F. Muschitiello, W. J. D'Andrea, A. Schmittner, T. J. Heaton, N. L. Balascio, N. deRoberts, *et al.*, Deep-water circulation changes lead North Atlantic climate during deglaciation. *Nat. Commun.* **10** (2019), doi:10.1038/s41467-019-09237-3.

37. J. A. Eddy, The Maunder Minimum. *Science*. **192**, 1189–1202 (1976).

38. F. Steinhilber, J. A. Abreu, J. Beer, I. Brunner, M. Christl, H. Fischer, *et al.*, 9,400 years of cosmic radiation and solar activity from ice cores and tree rings. *Proc. Natl. Acad. Sci.* **109**, 5967–5971 (2012).

39. R. Roth, F. Joos, A reconstruction of radiocarbon production and total solar irradiance from the Holocene ^{14}C and CO_2 records: implications of data and model uncertainties. *Clim. Past*. **9**, 1879–1909 (2013).

40. E. Bard, G. Raisbeck, F. Yiou, J. Jouzel, Solar irradiance during the last 1200 years based on cosmogenic nuclides. *Tellus B Chem. Phys. Meteorol.* **52**, 985–992 (2000).

41. F. Adolphi, R. Muscheler, A. Svensson, A. Aldahan, G. Possnert, J. Beer, *et al.*, Persistent link between solar activity and Greenland climate during the Last Glacial Maximum. *Nat. Geosci.* **7**, 662–666 (2014).

42. P. O'Hare, F. Mekhaldi, F. Adolphi, G. Raisbeck, A. Aldahan, E. Anderberg, *et al.*, Multiradionuclide evidence for an extreme solar proton event around 2,610 B.P. (~660 BC) . *Proc. Natl. Acad. Sci.* . **116** (2019), pp. 5961–5966.

43. G. A. Kovaltsov, A. Mishev, I. G. Usoskin, A new model of cosmogenic production of radiocarbon ^{14}C in the atmosphere. *Earth Planet. Sci. Lett.* **337**–**338**, 114–120 (2012).

44. J. Masarik, J. Beer, Simulation of particle fluxes and cosmogenic nuclide production in the Earth's atmosphere. *J. Geophys. Res. Atmos.* **104**, 12099–12111 (1999).

45. U. Siegenthaler, M. Heimann, H. Oeschger, ^{14}C Variations Caused by Changes in the Global Carbon Cycle. *Radiocarbon*. **22**, 177–191 (1980).

46. P. E. Damon, C. P. Sonett, in *The Sun in Time*, C. P. Sonett, M. S. Giampapa, M. S. Matthews, Eds. (University of Arizona Press, Tucson, AZ USA, 1991; https://ui.adsabs.harvard.edu/abs/1991suti.conf..360D), p. 360.

47. M. Vonmoos, J. Beer, R. Muscheler, Large variations in Holocene solar activity: Constraints from ^{10}Be in the Greenland Ice Core Project ice core. *J. Geophys. Res. Sp. Phys.* **111** (2006), doi:10.1029/2005JA011500.

48. L. Svalgaard, K. H. Schatten, Reconstruction of the Sunspot Group Number: The Backbone Method. *Sol. Phys.* **291**, 2653–2684 (2016).

49. J. H. Jungclaus, E. Bard, M. Baroni, P. Braconnot, J. Cao, L. P. Chini, *et al.*, The PMIP4 contribution to CMIP6 – Part 3: The last millennium, scientific objective, and experimental design for the PMIP4 *past1000* simulations. *Geosci. Model Dev.* **10**, 4005–4033 (2017).

50. G. Bond, B. Kromer, J. Beer, R. Muscheler, M. N. Evans, W. Showers, *et al.*, Persistent Solar Influence on North Atlantic Climate During the Holocene. *Science*. **294**, 2130–2136 (2001).

51. R. Muscheler, J. Beer, G. Wagner, C. Laj, C. Kissel, G. M. Raisbeck, *et al.*, Changes in the carbon cycle during the last deglaciation as indicated by the comparison of ^{10}Be and ^{14}C records. *Earth Planet. Sci. Lett.* **219**, 325–340 (2004).

52. A. Cauquoin, G. M. Raisbeck, J. Jouzel, E. Bard, No evidence for planetary influence on solar activity 330 000 years ago. *Astron. Astrophys.* **561**, A132 (2014).

53. W. R. Webber, P. R. Higbie, K. G. McCracken, Production of the cosmogenic isotopes ^{3}H, ^{7}Be, ^{10}Be, and ^{36}Cl in the Earth's atmosphere by solar and galactic cosmic rays. *J. Geophys. Res. Sp. Phys.* **112** (2007), doi:10.1029/2007JA012499.

54. U. Büntgen, L. Wacker, J. D. Galván, S. Arnold, D. Arseneault, M. Baillie, *et al.*, Tree rings reveal globally coherent signature of cosmogenic radiocarbon events in 774 and 993 CE. *Nat. Commun.* **9**, 3605 (2018).

55. M. Sigl, M. Winstrup, J. R. McConnell, K. C. Welten, G. Plunkett, F. Ludlow, *et al.*, Timing and climate forcing of volcanic eruptions for the past 2,500 years. *Nature*. **523**, 543–549 (2015).

56. K. G. McCracken, J. Beer, Long-term changes in the cosmic ray intensity at Earth, 1428–2005. *J. Geophys. Res. Sp. Phys.* **112** (2007), doi:10.1029/2006JA012117.

57. A.-M. Berggren, J. Beer, G. Possnert, A. Aldahan, P. Kubik, M. Christl, *et al.*, A 600-year annual ^{10}Be record from the NGRIP ice core, Greenland. *Geophys. Res. Lett.* **36** (2009), doi:10.1029/2009GL038004.

58. D. Gubbins, A. L. Jones, C. C. Finlay, Fall in Earth's Magnetic Field Is Erratic. *Science*. **312**, 900–902 (2006).

59. E. Thellier, O. Thellier, Sur l'intensité du champ magnétique terrestre, en France, trois siècles avant les premières mesures directes. Application, au problème de la désaimantation du globe. *C. R. Acad. Sci. Paris*. **214**, 382–384 (1942).

60. M. C. Brown, F. Donadini, M. Korte, A. Nilsson, K. Korhonen, A. Lodge, *et al.*, GEOMAGIA50.v3: 1. general structure and modifications to the archeological and volcanic database. *Earth, Planets Sp.* **67**, 83 (2015).

61. C. Laj, C. Kissel, A. Mazaud, J. E. T. Channell, J. Beer, North Atlantic palaeointensity stack since 75ka (NAPIS–75) and the duration of the Laschamp event. *Philos. Trans. R. Soc. London. Ser. A Math. Phys. Eng. Sci.* **358**, 1009–1025 (2000).

62. N. Thouveny, J. Carcaillet, E. Moreno, G. Leduc, D. Nérini, Geomagnetic moment variation and paleomagnetic excursions since 400 kyr BP: a stacked record from sedimentary sequences of the Portuguese margin. *Earth Planet. Sci. Lett.* **219**, 377–396 (2004).

63. N. R. Nowaczyk, U. Frank, J. Kind, H. W. Arz, A high-resolution paleointensity stack of the past 14 to 68 ka from Black Sea sediments. *Earth Planet. Sci. Lett.* **384**, 1–16 (2013).

64. S. Panovska, M. Korte, C. G. Constable, One Hundred Thousand Years of Geomagnetic Field Evolution. *Rev. Geophys.* **57**, 1289–1337 (2019).

65. I. Lascu, J. M. Feinberg, J. A. Dorale, H. Cheng, R. L. Edwards, Age of the Laschamp excursion determined by U-Th dating of a speleothem geomagnetic record from North America. *Geology*. **44**, 139–142 (2016).

66. G. A. Glatzmaiers, P. H. Roberts, A three-dimensional self-consistent computer simulation of a geomagnetic field reversal. *Nature*. **377**, 203–209 (1995).

67. W. Elsasser, E. P. Ney, J. R. Winckler, Cosmic-Ray Intensity and Geomagnetism. *Nature*. **178**, 1226–1227 (1956).

68. S. V Poluianov, G. A. Kovaltsov, A. L. Mishev, I. G. Usoskin, Production of cosmogenic isotopes ^{7}Be, ^{10}Be, ^{14}C, ^{22}Na, and ^{36}Cl in the atmosphere: Altitudinal profiles of yield functions. *J. Geophys. Res. Atmos.* **121**, 8125–8136 (2016).

69. E. Bard, B. Hamelin, R. G. Fairbanks, A. Zindler, Calibration of the ^{14}C timescale over the past 30,000 years using mass spectrometric U–Th ages from Barbados corals. *Nature*. **345**, 405–410 (1990).

70. K. Hughen, S. Lehman, J. Southon, J. Overpeck, O. Marchal, C. Herring, *et al.*, ^{14}C Activity and Global Carbon Cycle Changes over the Past 50,000 Years. *Science*. **303**, 202–207 (2004).

71. R. Muscheler, J. Beer, P. W. Kubik, H.-A. Synal, Geomagnetic field intensity during the last 60,000 years based on ^{10}Be and ^{36}Cl from the Summit ice cores and ^{14}C. *Quat. Sci. Rev.* **24**, 1849–1860 (2005).

72. J. E. T. Channell, D. A. Hodell, S. J. Crowhurst, L. C. Skinner, R. Muscheler, Relative paleointensity (RPI) in the latest Pleistocene (10–45 ka) and implications for deglacial atmospheric radiocarbon. *Quat. Sci. Rev.* **191**, 57–72 (2018).

73. G. M. Raisbeck, F. Yiou, D. Bourles, C. Lorius, J. Jouzel, N. I. Barkov, Evidence for two intervals of enhanced ^{10}Be deposition in Antarctic ice during the last glacial period. *Nature*. **326**, 273–277 (1987).

74. G. M. Raisbeck, A. Cauquoin, J. Jouzel, A. Landais, J.-R. Petit, V. Y. Lipenkov, *et al.*, An improved north–south synchronization of ice core records around the 41 kyr ^{10}Be peak. *Clim. Past*. **13**, 217–229 (2017).

75. M. Frank, B. Schwarz, S. Baumann, P. W. Kubik, M. Suter, A. Mangini, A 200 kyr record of cosmogenic radionuclide production rate and geomagnetic field intensity from ^{10}Be in globally stacked deep-sea sediments. *Earth Planet. Sci. Lett.* **149**, 121–129 (1997).

76. Q. Simon, N. Thouveny, D. L. Bourlès, J.-P. Valet, F. Bassinot, Cosmogenic ^{10}Be production records reveal dynamics of geomagnetic dipole moment (GDM) over the Laschamp excursion (20–60 ka). *Earth Planet. Sci. Lett.* **550**, 116547 (2020).

77. A. Dinauer, F. Adolphi, F. Joos, Mysteriously high Δ^{14}C of the glacial atmosphere: influence of ^{14}C production and carbon cycle changes. *Clim. Past*. **16**, 1159–1185 (2020).

78. C. Laj, C. Kissel, J. Beer, High Resolution Global Paleointensity Stack Since 75 kyr (GLOPIS-75) Calibrated to Absolute Values. *Timescales Paleomagn. F.* (2004), pp. 255–265.

79. F. Adolphi, C. Bronk Ramsey, T. Erhardt, R. L. Edwards, H. Cheng, C. S. M. Turney, *et al.*, Connecting the Greenland ice-core and U/Th timescales via cosmogenic radionuclides: testing the synchroneity of Dansgaard–Oeschger events. *Clim. Past*. **14**, 1755–1781 (2018).

80. P. Köhler, R. Muscheler, H. Fischer, A model-based interpretation of low-frequency changes in the carbon cycle during the last 120,000 years and its implications for the reconstruction of atmospheric $\Delta^{14}C$. *Geochemistry, Geophys. Geosystems*. **7** (2006), doi:10.1029/2005GC001228.

81. Y. Lao, R. F. Anderson, W. S. Broecker, S. E. Trumbore, H. J. Hofmann, W. Wolfli, Increased production of cosmogenic ^{10}Be during the Last Glacial Maximum. *Nature*. **357**, 576–578 (1992).

82. E. Bard, Geochemical and geophysical implications of the radiocarbon calibration. *Geochim. Cosmochim. Acta*. **62**, 2025–2038 (1998).

83. S. P. E. Blockley, C. S. Lane, M. Hardiman, S. O. Rasmussen, I. K. Seierstad, J. P. Steffensen, *et al.*, Synchronisation of palaeoenvironmental records over the last 60,000 years, and an extended INTIMATE event stratigraphy to 48,000 b2k. *Quat. Sci. Rev.* **36**, 2–10 (2012).

84. U. Heikkilä, J. Beer, J. Feichter, Meridional transport and deposition of atmospheric ^{10}Be. *Atmos. Chem. Phys.* **9**, 515–527 (2009).

85. F. Adolphi, R. Muscheler, Synchronizing the Greenland ice core and radiocarbon timescales over the Holocene-Bayesian wiggle-matching of cosmogenic radionuclide records . *Clim. Past* . **12** (2016), pp. 15–30.

86. C. Bronk Ramsey, P. Albert, S. Blockley, M. Hardiman, C. Lane, A. Macleod, *et al.*, Integrating timescales with time-transfer functions: a practical approach for an INTIMATE database. *Quat. Sci. Rev.* **106**, 67–80 (2014).

87. M. Blaauw, J. A. Christen, Flexible paleoclimate age-depth models using an autoregressive gamma process. *Bayesian Anal.* **6**, 457–474 (2011).

88. C. Bronk Ramsey, Deposition models for chronological records. *Quat. Sci. Rev.* **27**, 42–60 (2008).

89. J. Haslett, A. Parnell, A Simple Monotone Process with Application to Radiocarbon-Dated Depth Chronologies. *J. R. Stat. Soc. Ser. C (Applied Stat.* **57**, 399–418 (2008).

90. L. Bazin, A. Landais, B. Lemieux-Dudon, H. Toyé Mahamadou Kele, D. Veres, F. Parrenin, *et al.*, An optimized multi-proxy, multi-site Antarctic ice and gas orbital chronology (AICC2012): 120–800 ka. *Clim. Past*. **9**, 1715–1731 (2013).

91. C. Bronk Ramsey, P. G. Albert, S. P. E. Blockley, M. Hardiman, R. A. Housley, C. S. Lane, *et al.*, Improved age estimates for key Late Quaternary European tephra horizons in the RESET lattice. *Quat. Sci. Rev.* **118**, 18–32 (2015).

92. C. Buizert, M. Sigl, M. Severi, B. R. Markle, J. J. Wettstein, J. R. McConnell, *et al.*, Abrupt ice-age shifts in southern westerly winds and Antarctic climate forced from the north. *Nature*. **563**, 681–685 (2018).

93. S. O. Rasmussen, K. K. Andersen, A. M. Svensson, J. P. Steffensen, B. M. Vinther, H. B. Clausen, *et al.*, A new Greenland ice core chronology for the last glacial termination. *J. Geophys. Res. Atmos.* **111** (2006), doi:10.1029/2005JD006079.

94. M. Sigl, T. J. Fudge, M. Winstrup, J. Cole-Dai, D. Ferris, J. R. McConnell, *et al.*, The WAIS Divide deep ice core WD2014 chronology – Part 2: Annual-layer counting (0–31 ka BP). *Clim. Past*. **12**, 769–786 (2016).

95. A. Svensson, D. Dahl-Jensen, J. P. Steffensen, T. Blunier, S. O. Rasmussen, B. M. Vinther, *et al.*, Bipolar volcanic synchronization of abrupt climate change in Greenland and Antarctic ice cores during the last glacial period. *Clim. Past*. **16**, 1565–1580 (2020).

96. D. Veres, L. Bazin, A. Landais, H. Toyé Mahamadou Kele, B. Lemieux-Dudon, F. Parrenin, *et al.*, The Antarctic ice core chronology (AICC2012): an optimized multi-parameter and multi-site dating approach for the last 120 thousand years. *Clim. Past*. **9**, 1733–1748 (2013).

97. EPICA Community Members, One-to-one coupling of glacial climate variability in Greenland and Antarctica. *Nature*. **444**, 195–198 (2006).

98. C. Buizert, K. M. Cuffey, J. P. Severinghaus, D. Baggenstos, T. J. Fudge, E. J. Steig, *et al.*, The WAIS Divide deep ice core WD2014 chronology – Part 1: Methane synchronization (68–31 ka BP) and the gas age–ice age difference. *Clim. Past*. **11**, 153–173 (2015).

99. P. Friedlingstein, M. W. Jones, M. O'Sullivan, R. M. Andrew, J. Hauck, G. P. Peters, *et al.*, Global Carbon Budget 2019. *Earth Syst. Sci. Data*. **11**, 1783–1838 (2019).

100. B. Bereiter, S. Eggleston, J. Schmitt, C. Nehrbass-Ahles, T. F. Stocker, H. Fischer, *et al.*, Revision of the EPICA Dome C CO_2 record from 800 to 600 kyr before present. *Geophys. Res. Lett.* **42**, 542–549 (2015).

101. P. Ciais, A. Tagliabue, M. Cuntz, L. Bopp, M. Scholze, G. Hoffmann, *et al.*, Large inert carbon pool in the terrestrial biosphere during the Last Glacial Maximum. *Nat. Geosci.* **5**, 74–79 (2012).

102. A. Jeltsch-Thömmes, G. Battaglia, O. Cartapanis, S. L. Jaccard, F. Joos, Low terrestrial carbon storage at the Last Glacial Maximum: constraints from multi-proxy data. *Clim. Past*. **15**, 849–879 (2019).

103. Z. Shi, S. D. Allison, Y. He, P. A. Levine, A. M. Hoyt, J. Beem-Miller, *et al.*, The age distribution of global soil carbon inferred from radiocarbon measurements. *Nat. Geosci.* **13**, 555–559 (2020).

104. L. C. Skinner, F. Primeau, E. Freeman, M. de la Fuente, P. A. Goodwin, J. Gottschalk, *et al.*, Radiocarbon constraints on the glacial ocean circulation and its impact on atmospheric CO_2. *Nat. Commun.* **8**, 16010 (2017).

105. L. Stott, J. Southon, A. Timmermann, A. Koutavas, Radiocarbon age anomaly at intermediate water depth in the Pacific Ocean during the last deglaciation.

Paleoceanography. **24** (2009), doi:10.1029/2008PA001690.

106. T. A. Ronge, R. Tiedemann, F. Lamy, P. Köhler, B. V Alloway, R. De Pol-Holz, *et al.*, Radiocarbon constraints on the extent and evolution of the South Pacific glacial carbon pool. *Nat. Commun.* **7**, 11487 (2016).

107. J. Hasenclever, G. Knorr, L. H. Rüpke, P. Köhler, J. Morgan, K. Garofalo, *et al.*, Sea level fall during glaciation stabilized atmospheric CO_2 by enhanced volcanic degassing. *Nat. Commun.* **8**, 15867 (2017).

108. S. A. Marcott, T. K. Bauska, C. Buizert, E. J. Steig, J. L. Rosen, K. M. Cuffey, *et al.*, Centennial-scale changes in the global carbon cycle during the last deglaciation. *Nature*. **514**, 616–619 (2014).

109. T. K. Bauska, D. Baggenstos, E. J. Brook, A. C. Mix, S. A. Marcott, V. V Petrenko, *et al.*, Carbon isotopes characterize rapid changes in atmospheric carbon dioxide during the last deglaciation. *Proc. Natl. Acad. Sci.* **113**, 3465–3470 (2016).

110. T. K. Bauska, E. J. Brook, S. A. Marcott, D. Baggenstos, S. Shackleton, J. P. Severinghaus, *et al.*, Controls on Millennial-Scale Atmospheric CO_2 Variability During the Last Glacial Period. *Geophys. Res. Lett.* **45**, 7731–7740 (2018).

111. J. Vandenberghe, H. M. French, A. Gorbunov, S. Marchenko, A. A. Velichko, H. Jin, *et al.*, The Last Permafrost Maximum (LPM) map of the Northern Hemisphere: permafrost extent and mean annual air temperatures, 25–17 ka BP. *Boreas*. **43**, 652–666 (2014).

112. F. Rostek, E. Bard, Hydrological changes in eastern europe during the last 40,000 yr inferred from biomarkers in Black Sea Sediments. *Quat. Res.* **80**, 502–509 (2013).

113. M. Winterfeld, G. Mollenhauer, W. Dummann, P. Köhler, L. Lembke-Jene, V. D. Meyer, *et al.*, Deglacial mobilization of pre-aged terrestrial carbon from degrading permafrost. *Nat. Commun.* **9**, 3666 (2018).

114. T. Tesi, F. Muschitiello, R. H. Smittenberg, M. Jakobsson, J. E. Vonk, P. Hill, *et al.*, Massive remobilization of permafrost carbon during post-glacial warming. *Nat. Commun.* **7**, 13653 (2016).

115. J. Martens, B. Wild, C. Pearce, T. Tesi, A. Andersson, L. Bröder, *et al.*, Remobilization of Old Permafrost Carbon to Chukchi Sea Sediments During the End of the Last Deglaciation. *Global Biogeochem. Cycles*. **33**, 2–14 (2019).

116. V. D. Meyer, J. Hefter, P. Köhler, R. Tiedemann, R. Gersonde, L. Wacker, *et al.*, Permafrost-carbon mobilization in Beringia caused by deglacial meltwater runoff, sea-level rise and warming. *Environ. Res. Lett.* **14**, 085003 (2019).

117. J. Martens, B. Wild, F. Muschitiello, M. O'Regan, M. Jakobsson, I. Semiletov, *et al.*, Remobilization of dormant carbon from Siberian-Arctic permafrost during three past warming events. *Sci. Adv.* **6**, eabb6546 (2020).

118. P. Köhler, G. Knorr, E. Bard, Permafrost thawing as a possible source of abrupt carbon release at the onset of the Bølling/Allerød. *Nat. Commun.* **5**, 5520 (2014).

119. M. N. Dyonisius, V. V Petrenko, A. M. Smith, Q. Hua, B. Yang, J. Schmitt, *et al.*, Old carbon reservoirs were not important in the deglacial methane budget. *Science*. **367**, 907–

910 (2020).

120. M. Butzin, M. Prange, G. Lohmann, Radiocarbon simulations for the glacial ocean: The effects of wind stress, Southern Ocean sea ice and Heinrich events. *Earth Planet. Sci. Lett.* **235**, 45–61 (2005).

121. E. Bard, Correction of accelerator mass spectrometry ^{14}C ages measured in planktonic foraminifera: Paleoceanographic implications. *Paleoceanography*. **3**, 635–645 (1988).

122. E. D. Galbraith, E. Y. Kwon, D. Bianchi, M. P. Hain, J. L. Sarmiento, The impact of atmospheric *p*CO2 on carbon isotope ratios of the atmosphere and ocean. *Global Biogeochem. Cycles*. **29**, 307–324 (2015).

123. T. DeVries, F. Primeau, An improved method for estimating water-mass ventilation age from radiocarbon data. *Earth Planet. Sci. Lett.* **295**, 367–378 (2010).

124. K. Matsumoto, J. L. Sarmiento, R. M. Key, O. Aumont, J. L. Bullister, K. Caldeira, *et al.*, Evaluation of ocean carbon cycle models with data-based metrics. *Geophys. Res. Lett.* **31** (2004), doi:10.1029/2003GL018970.

125. T. Tschumi, F. Joos, M. Gehlen, C. Heinze, Deep ocean ventilation, carbon isotopes, marine sedimentation and the deglacial CO_2 rise. *Clim. Past*. **7**, 771–800 (2011).

126. M. Butzin, P. Köhler, G. Lohmann, Marine radiocarbon reservoir age simulations for the past 50,000 years. *Geophys. Res. Lett.* **44**, 8473–8480 (2017).

127. N. Zhao, O. Marchal, L. Keigwin, D. Amrhein, G. Gebbie, A Synthesis of Deglacial Deep-Sea Radiocarbon Records and Their (In)Consistency With Modern Ocean Ventilation. *Paleoceanogr. Paleoclimatology*. **33**, 128–151 (2018).

128. S. Danilov, D. Sidorenko, Q. Wang, T. Jung, The Finite-volumE Sea ice–Ocean Model (FESOM2). *Geosci. Model Dev.* **10**, 765–789 (2017).

129. A. Cooper, C. S. M. Turney, J. Palmer, A. Hogg, M. McGlone, J. Wilmshurst, *et al.*, A global environmental crisis 42,000 years ago. *Science*. **371**, 811–818 (2021).

130. M. A. Plummer, F. M. Phillips, J. Fabryka-Martin, H. J. Turin, P. E. Wigand, P. Sharma, Chlorine-36 in Fossil Rat Urine: An Archive of Cosmogenic Nuclide Deposition During the Past 40,000 Years. *Science*. **277**, 538–541 (1997).

Acknowledgments: We thank Ed Rhodes and Shaun Quegan for insightful comments which improved our proposal; Florian Adolphi for discussion on ^{14}C production rate reconstructions; Lee Johnstone and Sadie Renwick for help with the illustrations; and Clare Pratt, Jeremy Ely, and Sophie Whyte for feedback on earlier drafts. **Funding**: TJH was funded by a Leverhulme Trust Fellowship RF-2019-140\9. EB is supported by EQUIPEX ASTER-CEREGE and ANR CARBOTRYDH. MB is supported by the German Federal Ministry of Education and Research (BMBF), as Research for Sustainability initiative (FONA); www.fona.de through the PalMod project (Grant 01LP1919A). RM was funded by the Swedish Research Council (Grant DNR2013-8421 and DNR2018-05469). CBR is supported by the Natural Environment Research Council (NERC) as part of the National Environmental Isotope Facility (NEIF). PJR was funded by the UKRI Natural Environment Research Council (Grant NE/M004619/1). **Author Contributions**: All authors contributed to the development of ideas for the review, the writing of

initial drafts and subsequent revision. **Competing interests**: Authors declare no competing interests. **Data and materials availability**: Data for Figure 6 are accessible at https://doi.pangaea.de/10.1594/PANGAEA.928497. All other data are available in the accompanying references.

Fig. 7. The production and subsequent distribution of ^{14}C and other cosmogenic radionuclides throughout the Earth system. Production of ^{14}C and other cosmogenic nuclides (such as ^{10}Be and ^{36}Cl) occurs mainly in the stratosphere and upper layers of the troposphere driven by incoming galactic cosmic rays. While the galactic cosmic ray flux is assumed constant and isotropic, nuclide production rates are spatio-temporally modulated by magnetic shielding influenced by both the Sun's activity and the strength of the Earth's magnetic field. Further nuclide production can result from the release of solar energetic particles during extreme solar storms. After production, the nuclides are dispersed through the Earth system. In the case of ^{14}C, this dispersal occurs via the carbon cycle resulting in different ratios of ^{14}C, compared to stable ^{12}C, in its various oceanic and terrestrial compartments – the blue color scale shows the approximate $^{14}C/^{12}C$ ratios relative to the northern troposphere. Past levels of radionuclides are recorded in a range of archives. For ^{14}C these archives include tree-rings, stalagmites, corals, and lacustrine and marine sediments containing foraminifera; while ^{10}Be and ^{36}Cl are recorded in ice cores and sediments. Simultaneous comparison of ^{14}C levels in the different carbon cycle compartments, used alongside other cosmogenic nuclides, informs us about the climate system and carbon cycle processes over time, and provides insight into the Sun and the geodynamo.

Fig. 8. IntCal20 NH estimate of atmospheric ^{14}C variations (expressed as $\Delta^{14}C$) over the last 55,000 years compared with the previous IntCal13 estimate. The additional ^{14}C detail in the IntCal20 curve is due to the availability of new archives, combined with recent advances in measurement and modeling. Panel A: A plot of the posterior mean (solid line) and 2σ credible interval (shaded area) of the curves. Note in particular the significant increase in $\Delta^{14}C$ identified in IntCal20 around the Laschamps geomagnetic excursion (~41,000 cal BP) observed in Hulu Cave. Panel B: The 774-775 CE Event (1176 – 1175 cal BP) showing the sharp increase in $\Delta^{14}C$ identified with the annual data of IntCal20. This event was not observed in the lower resolution IntCal13. Shown are a sample of individual posterior IntCal20 curve realizations that enable a user to access covariance information (variously-colored lines); and the summarized posterior mean (solid blue line) and 2σ credible interval (shaded blue). Panel C: The extension of annually-resolved data into the Younger-Dryas provides a much more detailed ^{14}C estimate during a key period of climate change than was available with the IntCal13 curve. Individual IntCal20 curve realizations are plotted (variously-colored lines) together with the posterior IntCal13 and IntCal20 means and 2σ credible intervals.

Fig. 9. Direct and indirect data on past changes in solar activity. Panel A: A reconstruction of the solar shielding of galactic cosmic rays based on neutron monitor measurements (56). Panel B: Group sunspot number reconstruction (48). Panel C: The IntCal20 NH $\Delta^{14}C$ estimate (mean ± 2σ) (6). It mirrors the ups and down in solar activity and shows the "^{14}C-Suess effect" i.e. the decrease of atmospheric ^{14}C in relation to the stable ^{12}C that began at the start of the industrial revolution in 1850 and is due to the massive release of ^{14}C-free CO_2 from the burning of fossil fuel (4). Panel D: Annual ^{10}Be data (57) shows significant weather noise but has a better potential to preserve the amplitude of the variations (±20%) connected to the 11-yr solar cycle and show the cycle's influence on the shielding of galactic cosmic rays. The grey bands show the

period of the Maunder minimum around 1700, the Dalton minimum around 1800 and the shorter 1900 low solar activity period.

Fig. 10. Comparison of the IntCal20 atmospheric $\Delta^{14}C$ estimate with paleomagnetic and cosmogenic radionuclide model-based reconstructions. The measurement-based IntCal20 (blue) is shown alongside Bern3D model-based $\Delta^{14}C$ reconstructions for which ^{14}C production rates were calculated using geomagnetic field intensity (orange and brown) and ^{10}Be (purple) (77). Clear divergences are seen in the size of the atmospheric $\Delta^{14}C$ rise corresponding to the Laschamps geomagnetic excursion (shaded area from 42,000 – 40,000 cal BP) between the IntCal20 estimate and the paleomagnetic- and ^{10}Be-based reconstructions. The differences extend to the beginning of the Holocene. The paleomagnetic reconstructions are based upon the Global Paleointensity Stack (GLOPIS) (78), and a high resolution combination of measurements from the Black Sea (63). The ^{10}Be reconstruction is based on a combination of radionuclide data from different ice cores including GRIP and GISP (79). All model-based reconstructions assume a constant preindustrial carbon cycle. Due to the wide spread of the various model-based reconstructions, it is not possible to conclude if the differences from the measurement-based IntCal20 atmospheric $\Delta^{14}C$ estimate are due to limitations and uncertainties in the paleomagnetic- and ^{10}Be -reconstructions of ^{14}C production rate, or a lack of knowledge in the ^{14}C cycle during the last glacial period.

Fig. 11. Schematic of the direct synchronization methods for records spanning the last 55,000 years. These synchronization methods can be used to enhance or replace climate-based tuning of chronologies. The central circle shows the records contained within the IntCal20 dataset and directly synchronized through the statistical processes involved in the compilation using ^{14}C. Radiocarbon is also the primary method for relating terrestrial environmental and archaeological records to the primary IntCal ^{14}C-based timescale. Variation in marine offsets means that other methods such as volcanic ash shards (tephra) and other event-based methods are normally used to synchronize marine records. The link to ice-core chronologies is provided by looking at the relationship between ^{10}Be and ^{14}C, while between ice cores we can use a combination of local events and global signals, in particular CH_4, sulfur maxima, and ^{10}Be. Volcanic tephra layers provide a check and give precise synchronization at specific points in the chronology: these can be found in sedimentary records, ice cores, and some archaeological sites.

Fig. 12. Radiocarbon distributions in the past Atlantic. Depletion of dissolved ^{14}C with respect to the contemporaneous atmosphere for meridional sections along 30°W at 21,000 cal BP (around the Last Glacial Maximum, top) and 42,000 cal BP (the onset of the Laschamps geomagnetic excursion, bottom) according to an ocean general circulation model (12, 126). This model was run from 55,000 cal BP to 0 cal BP, forced with IntCal20 atmospheric $\Delta^{14}C$ and ice core CO_2 (6). Each panel displays the median of nine simulations. Depletion is expressed in terms of ^{14}C age. Low ^{14}C concentrations translate to high ^{14}C ages and vice versa. In both panels the average ocean circulation is the same. The differences between 21,000 cal BP and 42,000 cal BP are instead due to changes in atmospheric $\Delta^{14}C$ levels in combination with different leads and lags between these atmospheric $\Delta^{14}C$ changes and their oceanic uptake and dispersal.